Since January 2020 Elsevier has created a COVID-19 resource centre with free information in English and Mandarin on the novel coronavirus COVID-19. The COVID-19 resource centre is hosted on Elsevier Connect, the company's public news and information website.

Ecological Informatics 71 (2022) 101809

Contents lists available at ScienceDirect

Ecological Informatics

journal homepage: www.elsevier.com/locate/ecolinf

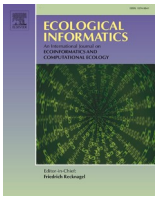

Assessment of the dynamics of urban surface temperatures and air pollution related to COVID-19 in a densely populated City environment in East Java

Purwanto Purwanto [a,*], Ike Sari Astuti [a], Fatchur Rohman [b], Kresno Sastro Bangun Utomo [a], Yulius Eka Aldianto [a]

[a] Department of Geography, Faculty of Social Sciences, Universitas Negeri Malang, No. 5 Semarang Road, Malang 65145, Indonesia
[b] Department of Biology, Faculty of Mathematics and Natural Sciences, Universitas Negeri Malang, No. 5 Semarang Road, Malang 65145, Indonesia

ARTICLE INFO

Keywords:
COVID-19
Partial lockdown
Urban surface temperatures
Spatial downscaling
Air pollution
GIS & remote sensing

ABSTRACT

The COVID-19 pandemic that has hit the whole world has caused losses in various aspects. Several countries have implemented lockdowns to curb the spread of the SARS-CoV-2 virus that caused death. However, for developing countries such as Indonesia, it is not suitable for lockdown because it considers the economic recession. Instead, the Large-scale Social Restrictions (LSSR) regulation is applied, the same as the partial lockdown. Thus, it is hypothesized that implementing LSSR that limits anthropogenic activities can reduce heat emissions and air pollution. Utilization of remote sensing data such as Terra-MODIS LST and Sentinel-5P images to investigate short-term trends (i.e., comparison between baseline year and COVID-19 year) in surface temperature, Surface Urban Heat Islands Intensity (SUHII), and air pollution such as NO_2, CO, and O_3 in Malang City and Surabaya City, East Java Province. Spatial downscaling of LST using the Random Forest Regression technique was also carried out to transform the spatial resolution of the Terra-MODIS LST image to make it feasible on a city scale. Raster re-gridding was also implemented to refine the Sentinel-5P spatial resolution. The accuracy of LST spatial downscaling results is quite satisfactory in both cities. Surface temperatures in both cities slightly decreased (below 1 °C) during LSSR was applied ($P < 0.05$). SUHII in both cities experienced a slight increase in both cities during LSSR. NO_2 gas was reduced significantly ($P < 0.05$) in Malang City (~38%) and Surabaya City (~28%) during LSSR phase due to reduced vehicle traffic and restrictions on anthropogenic activities. However, CO and O_3 gases did not indicate anomaly during LSSR. Moreover, this study provides insight into the correlation between SUHII change and the distribution of air pollution in both cities during the pandemic year. Air temperature and wind speed are also added as meteorological factors to examine their effect on air pollution. The proposed models of spatial downscaling LST and re-gridding satellite-based air pollution can help decision-makers control local air quality in the long and short term in the future. In addition, this model can also be applied to other ecological research, especially the input variables for ecological spatial modeling.

1. Introduction

COVID-19 has hit the world, causing losses in many aspects. COVID-19 was first identified in Wuhan City, Hubei Province, China, in December 2019 (Huang et al., 2020; Q. Li et al., 2020). The outbreak was caused by Severe Acute Respiratory Syndrome COVID-19 virus 2 (SARS-CoV-2) (Desjardins et al., 2020; WHO, 2020b). >140 countries have confirmed the case categorized as a pandemic. As of June 30th, 2020, globally, the total confirmed cases reached 10,245,317, with 502,123 deaths (Roser et al., 2020). countries have carried out various measures to inhibit the spread of COVID-19 by implementing social distancing, physical distancing, and lockdown (Galvin et al., 2020; WHO, 2020a). Most countries have implemented lockdown to inhibit the spread of this virus (Mandal and Pal, 2020). This regulation effectively curbed the spread of the SARS-CoV-2 virus because anthropogenic activities are very limited. Still, it requires the readiness of a country regarding food subsidies from the government and the mental readiness of the community. This may not be in line in developing countries, especially Indonesia, so applying semi-lockdown/partial lockdown is more suitable.

Indonesia implements several partial lockdown schemes, including the Large-Scale Social Restrictions (LSSR) policy, Local Social

* Corresponding author.
E-mail address: purwanto.fis@um.ac.id (P. Purwanto).

https://doi.org/10.1016/j.ecoinf.2022.101809
Received 26 March 2022; Received in revised form 5 September 2022; Accepted 5 September 2022
Available online 8 September 2022

Restrictions policy, and the Implementation of Restrictions on Community Activities Micro-scale policy. From this perspective, geographically, they can be called multi-scale anthropogenic space restrictions. East Java is one of the provinces that implements LSSR in some urban areas because of the second-highest number of cases on the national scale as it is known that, in general, urban areas as the center of the spread of COVID-19. Surabaya and Malang are two cities in East Java that implement LSSR.

LSSR Surabaya was held from April 28th to June 7th, 2020 (Toharudin et al., 2020), while in Malang from May 17th to May 30th, 2020. During this LSSR, restrictions were placed on several activities such as religious, public, socio-cultural, and transportation (Jatim, 2020). This restriction is the same as a partial lockdown in which community activities still exist; however, it decreased intensity. Industrial operations are still running, but health protocols are more emphasized using a shifting work system (i.e., morning, afternoon, and evening). In addition, traditional markets for the primary needs of the community are still open but apply an open-closed system (i.e., one day open, one day closed, etc.). Activities that are of medical importance are prioritized without any restrictions on movement. Land, water, and air vehicles outside the city are not allowed to enter the city unless an urgent need or an important assignment letter from the government is obtained. Entertainment, recreation, urban parks, and education are temporarily suspended. Restrictions on activities may affect economic and environmental conditions. The effect of restrictions on economic conditions may have a more negative impact, but such restrictions can reduce the adverse impact on the quality of the environment, namely micro-climate change due to anthropogenic activity (Mandal and Pal, 2020).

One of the urban environmental problems is the development of Urban Heat Islands (UHI) caused by land cover material and human activities. UHI accumulates heat in urban areas due to higher temperatures than in the surrounding suburbs and countryside. Generally, UHI can be categorized based on the methods and height of its formation, namely Atmospheric Urban Heat Islands (AUHI) and Surface Urban Heat Islands (SUHI). However, UHI is usually thought of as the atmospheric temperature. AUHI is divided into two layers, namely the Urban Canopy Layer (UCL), which is a layer of the urban atmosphere that is limited from the surface to the average building height, and the Urban Boundary Layer (UBL) is a layer above the UCL which is influenced by the urban surface (Voogt and Oke, 2003). UCL can be measured using in-situ sensors mounted on meteorological stations or sensor tracks on vehicles (Nichol et al., 2009; Schwarz et al., 2012; Voogt and Oke, 2003).

Meanwhile, UBL is observed through tower platforms, radiosondes, balloons, or aircraft mounted with special sensors. SUHI is the difference in brightness temperature of objects between urban and non-urban areas as measured by remote sensing satellite thermal sensors. More specifically, the remote sensor captures the spatial pattern of upwelling thermal radiance, also known as directional radiometric temperatures or directional brightness radiometric (Voogt and Oke, 2003). SUHI is measured indirectly, which means it requires consideration of atmospheric intervention and surface radiation characteristics that affect the emission and reflection of radiation in the electromagnetic spectrum detected by the sensor. In addition, AUHI correlates with SUHI but is measured empirically. Temperature advection is influenced by variations in the spatial configuration of urban surfaces, such as thermal and humidity properties, complex surfaces, and aerodynamic roughness which results in different energy balances and surface temperatures (Voogt and Oke, 2003). In addition, surface imperviousness, vegetation cover, and local climate zone are also important factors for the linear relationship between AUHI and SUHI (Gawuc et al., 2020). This is due to the high thermal inertia of the artificial surfaces compared to the natural surfaces. In addition, natural areas with abundant vegetation increase absolute humidity, so cooling rates are higher than in urban areas, which can cause near-ground air temperature inversion after sunset.

Land Surface Temperature (LST) is one of the important environmental variables for surface SUHI studies in urban areas. Land cover material with high heat energy absorption ability causes the temperature to increase because of low albedo (Berila and Isufi, 2021). Anthropogenic activities such as transportation, industrial, heating, and air conditioning emissions can affect surface UHI (Shi et al., 2019; Wang et al., 2018). An alarming increase in urban temperature can harm human health, especially young children, the elderly, and people with a history of respiratory disease. This issue must be highlighted because it is directly related to a new respiratory disease, i.e., COVID-19. Monitoring the formation of SUHI is easier by using remotely sensed data, especially LST parameters that have been widely implemented in urban climate studies and algorithm development innovations.

LST is acquired from remote sensing data, particularly from satellites with thermal sensors. Generally, previous research for LST-based environmental quality analysis uses Landsat ETM+ and TIRS (Thermal Infrared Sensors) for moderate-scale mapping studies (Lillesand and Kiefer, 2000). However, the biggest weakness in Landsat imagery data is prone to cloud coverage, with a percentage of 41.05% at the 30% CC threshold in wet tropical Southeast Asia (Li et al., 2018; Martinuzzi et al., 2007). Landsat also has a low temporal resolution (16 days) for the micro-scale landscape change study, so an alternative is needed to address this problem.

Atmospheric emissions from natural and anthropogenic sources can harm human health. Limited anthropogenic activities during the pandemic significantly improves global air quality and reduces local emissions. Furthermore, this is evident in large cities with high population density, which contributes to anthropogenic emissions. Lockdown regulations implemented during the pandemic reap significant results in reducing air pollution on a global scale (Das et al., 2020) and in some regions such as the United States (Berman and Ebisu, 2020), Southeast Asia (Metya et al., 2020), Indian (Singh and Chauhan, 2020a), China (Chen et al., 2020) investigated through ground-based station or remote sensing. Some of these studies indicate that reducing anthropogenic activity caused by lockdown regulations (partial or strict) plays an important role in air quality restoration.

The combination of ground-based measurement with remote sensing does offer an accurate estimate of surface air temperature and air pollution mass concentrations with adequate spatial and temporal variations. However, not all regions provide quality ground-based data, such as the number of observation stations and the completeness of the data. In addition, another problem is the low visual quality of the medium-scale thermal sensor remote sensing data (i.e., Landsat TIRS) due to intensive cloud formation in the equatorial region, particularly in Indonesia. Therefore, this study offers an LST downscaling process of Terra-MODIS LST imagery with a resolution of ~1 km because it provides daily temporal. Previous research reports that Terra-MODIS LST can be sharpened spatial resolution based on elevation, spectral band, and vegetation factors as an independent factor – certainly use a higher spatial resolution (Duan and Li, 2016; Peng et al., 2019; Wang et al., 2020a, 2020b; Yang et al., 2019). However, various spatial downscaling techniques are used for atmospheric studies, especially LST, e.g., spatial statistics, machine learning, artificial intelligence, etc. Sentinel-2 imagery is used as an independent variable for the urban scale because of its good spatial and temporal resolution. In addition, air pollution mapping emphasizes using remote sensing data in this paper. This research is rarely conducted in big cities in Indonesia, especially the cities with the densest population in East Java Province.

In this context, the main purpose of this paper is to investigate short-term trends in surface temperature accompanied by an analysis of SUHI intensity and air pollution such as nitrogen dioxide (NO_2), carbon monoxide (CO), and ozone (O_3) based on remote sensing in Malang City and Surabaya City. Mapping LST, SUHII, and air pollution with geospatial data focused on before, during, and after LSSR, especially using remote sensing data from particular satellites, are presented in this paper. Anomalies or changes are detected using a baseline year (i.e., 2019) and COVID-19 year (i.e., 2020). Spatial downscaling is conducted to sharpen LST information pixels-based to map LST and SUHI intensity

on an urban scale.

2. Materials and methods

2.1. Study area

The scope of this study covers two metropolitan cities in East Java Province, i.e., the City of Surabaya and the City of Malang (Fig. 1). Astronomically, Surabaya is located at 7.207° - 7.356° S and 112.62° - 112.808° E. Meanwhile, Malang is located at 7.911° - 8.051° S and 112.568° - 112.694° E. Geographically, Surabaya is a coastal city with a gentle topography at 38.2 ± 7.2 masl. Malang is a city flanked by a mountain complex at 504.5 ± 48.3 masl with varied topography but slightly wavy relief.

Surabaya's average annual ambient air temperature ranges from 24.26 °C to 32.74 °C. Malang is lower than Surabaya, with a minimum span of 18.55 °C and a maximum of 28.98 °C. On the other hand, Surabaya's annual rainfall is around 1790 mm, and Malang's is around 2210 mm. January to March and November to December are the months that receive the highest rainfall.

Surabaya is divided into several smaller administrative units (i.e., urban communities/wards) with 154 wards and Malang with 54 wards. Both cities are dominated by built-up land, with a ratio of 73% and 77% for Malang and Surabaya, respectively. Other land uses are agricultural land, pond land (especially in the eastern part of Surabaya), and several open spaces and green spaces. Surabaya City has a population of about 2,887,223 people with a population density of 8795 people/km^2 (BPS Kota Surabaya, 2021). Meanwhile, Malang City has 843,810 people with a high population density of 9582 people/km^2 (BPS Kota Malang, 2021). These two cities are the most densely populated in East Java Province. Residential areas will continue to grow and spread to suburban areas so that there can be a substantial increase in the population. In addition, the population is an important factor in the formation of SUHII, especially in major cities (Cui et al., 2016). This is associated with the rate of urbanization and reduced vegetation cover replaced by buildings, roads, parking lots, pavements, and other structures. Adequate infrastructure and the availability of public facilities trigger population mobility to meet the needs of life. The use of public and private transportation to industrial areas in both cities can contribute to air pollution. Coupled with the high population density in both cities, this triggers more intensive fuel-burning activities.

2.2. Data preparation and image pre-processing

2.2.1. Satellite LST product

Terra-Moderate Resolution Imaging Spectroradiometer (Terra-MODIS) imagery is used in this study, specifically MOD11A1_L3v006 products with a spatial resolution of ~1 km. This imagery product is level-3, specifically Land Surface Temperature (LST) daily Global information. The algorithm for generating LST uses split-windows. This algorithm can produce more accurate LST values and low sensitivity to uncertainty in-band emissions and instrument interference (Mao et al., 2005; Zhengming Wan and Dozier, 1996). Bands 31 and 32 on MODIS are used as variables of the algorithm. We get this data from a Google Earth Engine platform. Optical imagery data has been processed up to level-2 or level-3 in images with additional image-processing eliminates

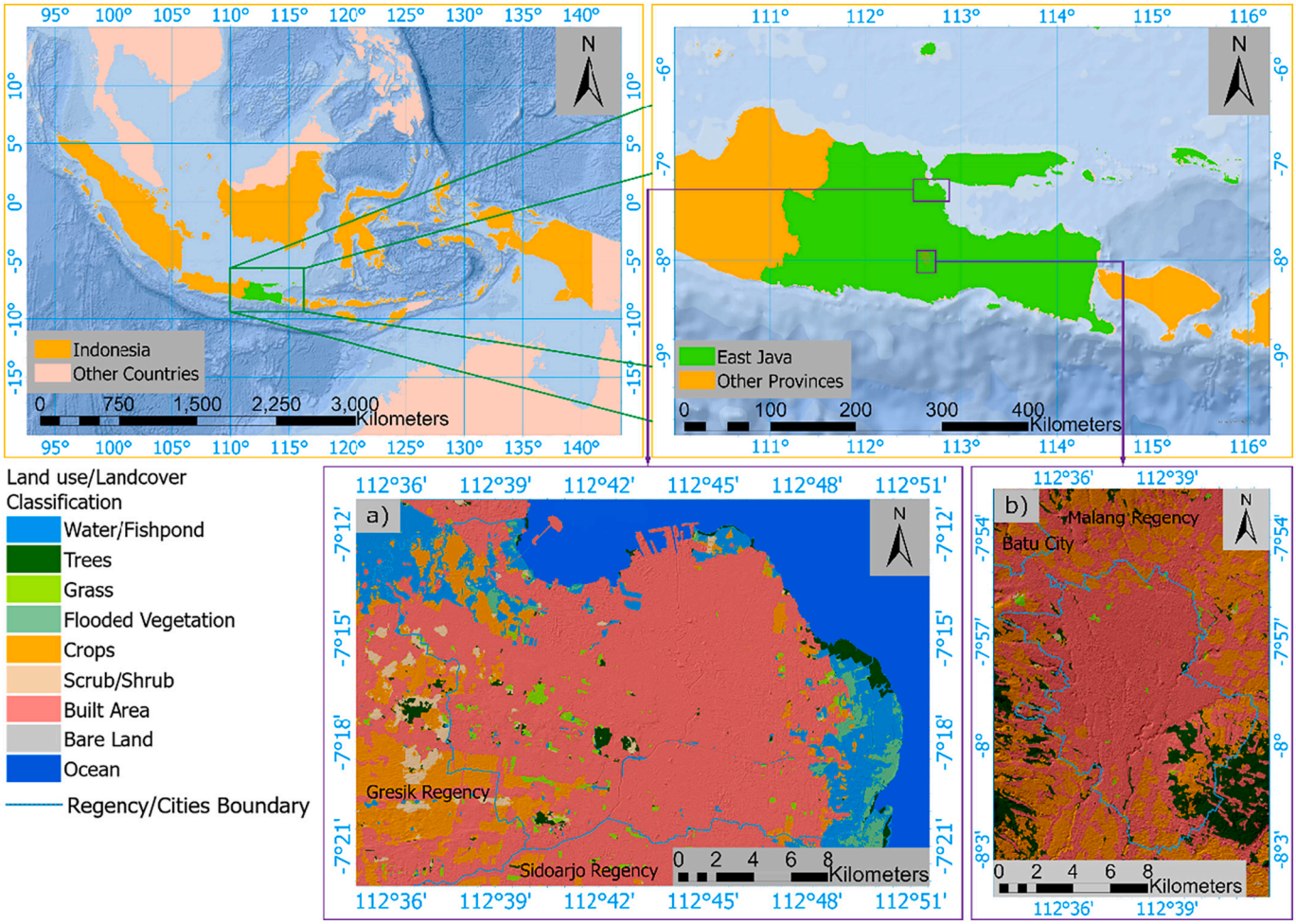

Fig. 1. Study area map in a) Surabaya City and b) Malang City with land use/landcover information.

clouds and can perform overlapping analysis on the same image scene. Still, it differs temporally so that null pixels can be updated with images with pixel values at the same location (Huntington et al., 2017).

2.2.2. Sentinel-2 satellite data

Sentinel-2 Multispectral Instrument (MSI) consists of two satellites, i.e., Sentinel-2A and Sentinel-2B carrying sensors at 10 m, 20 m, and 60 m spatial resolutions. Sentinel-2 provides a red-edge band capable of capturing substantial vegetation reflectance in the near-infrared. As shown in Table 1, the twin satellites have spectral bands with different wavelengths. Sentinel-2 satellite imagery acquired via Google Earth Engine platform (Google Earth Engine, 2012) to get a cloud-free image. The acquired image product is Level-2A reflectance data, which means that geometric, radiometric, and atmospheric corrections have been made. Then, the band sharpened at a spatial resolution of 20 m to 10 m using the High-Pass Filter technique (Chavez et al., 1991). This technique can sharpen the spatial resolution by extrapolating edge information from the high-resolution band to the lower spatial resolution band. In addition, this technique has several advantages, i.e., lower spectral information distortion compared to Hue-Intensity-Saturation and Principal Component Analysis techniques, can be applied to all or part of the bands, and low-frequency noise in higher spatial resolution images.

2.2.3. Independent variables for downscaling LST

Terra-MODIS LST and Sentinel-2 image data were taken before LSSR (30th March to 28th April 2020), during LSSR (29th April 2020 to 28th May 2020), and after LSSR (29th May 2020 to 27th June 2020) timeframes. We took the mean of the temporal measures with four-week accumulations in each period. Sentinel-2 data were used because Landsat thermal sensor data from before LSSR to after LSSR had poor visual quality due to clouds in Surabaya and Malang. As shown in Table 2, several reflectance bands and spectral indices were used for the LST downscaling process, including bands 2, 3, 4, 5, 6, 7, 8, 8a, 11, 12, NDVI (Normalized Difference Vegetation Index), NDWI (Normalized Difference Wetness Index), NDBI (Normalized Difference Built Index), and BSI (Bare Soil Index).

Meanwhile, elevation data obtained from IFSAR, TERRASAR-X, and ALOS-PALSAR data fusion results using the mass point data assimilation method, namely GMT-surface with the tension of 0.32 (BIG, 2008; Hell and Jakobsson, 2011). The image fusion result is called DEMNAS, acquired by the Geospatial Information Agency with a spatial resolution of 8.25 m in 2008. Terra-MODIS LST, Sentinel-2, and DEMNAS data are used for Spatial Downscaling LST from coarse-resolution to finer-resolution (i.e., 10 m). We performed spatial aggregation of elevation

Table 1
Spectral bands, spatial resolution, and wavelengths on Sentinel-2A and Sentinel-2B images.

Bands	Spatial Resolution (m)	Wavelength (nm)		Description
		Sentinel-2A	Sentinel-2B	
B1	60	443.9	442.3	Aerosol
B2	10	496.6	492.1	Blue
B3	10	560	559	Green
B4	10	664.5	665	Red
B5	20	703.9	703.8	Red Edge 1
B6	20	740.2	739.1	Red Edge 2
B7	20	782.5	779.7	Red Edge 3
B8	10	835.1	833	Near-infrared
B8A	20	864.8	864	Red Edge 4
B9	60	945	943.2	Water Vapor
B10	60	1373.5	1376.9	Cirrus
B11	20	1613.5	1610.4	Shortwave-infrared 1
B12	20	2202.4	2185.7	Shortwave-infrared 2

Table 2
Information on independent variables used for spatial downscaling of LST on Terra-MODIS LST imagery in the study area.

Variables	Spatial Resolution (m)	Description	Source
B2	10	Blue	Acquired from Sentinel-2 MSI
B3	10	Green	
B4	10	Red	
B5	20*	Red Edge 1	
B6	20*	Red Edge 2	
B7	20*	Red Edge 3	
B8	10	Near-infrared (NIR)	
B8A	20*	Red Edge 4	
B11	20*	Shortwave-infrared 1 (SWIR1)	
B12	20*	Shortwave-infrared 2 (SWIR2)	
NDVI	10	Normalized Difference Vegetation Index is a ratio between energy absorbed by vegetation in the red band and energy reflected near-infrared, usually for detecting vegetation surfaces.	$\frac{(NIR - RED)}{(NIR + RED)}$ (Purevdorj et al., 1998)
NDWI	10	Normalized Difference Water Index is an ratio between green and NIR to identify liquid water molecules in vegetation and water bodies because of their strong absorbing properties from the visible to infrared spectrum.	$\frac{(GREEN - NIR)}{(GREEN + NIR)}$ (Gao, 1996)
NDBI	10	Normalized Difference Built-up Index is a ratio for identifying artificial surfaces because it has a strong reflectance in the SWIR band to suppress the influence of vegetation surfaces from the NIR band.	$\frac{(SWIR - NIR)}{(SWIR + NIR)}$ (Zha et al., 2003)
BSI	10	Bare Soil Index uses blue, red, NIR, SWIR bands to identify soil variations. The index is calculated by the ratio between the SWIR and red bands to the Blue and NIR bands.	$\frac{((RED + SWIR) - (NIR + BLUE))}{((RED + SWIR) + (NIR + BLUE))}$ (Roy et al., 1996)
DEM	8.25*	Digital Elevation Model represents the vertical distance between the topography of	Aquired from DEMNAS

(continued on next page)

Table 2 (*continued*)

Variables	Spatial Resolution (m)	Description	Source
		the earth's surface (trees, building, and other objects are not included) and the reference point, namely sea level.	

* Resampled to 10 m.

data that follows the spatial resolution of Sentinel-2 data to be consistent, analyzable, and avoid errors during spatial downscaling.

2.2.4. Satellite air pollution product

Air pollution data were acquired from Sentinel-5 Precursor Tropospheric Monitoring Instrument imagery, which are. Available and easily accessible via the Google Earth Engine platform. Sentinel-5P spatial with resolution of around 0.01 arc degrees are high enough to study atmospheric concentration estimation with a metropolitan city-scale coverage. Air pollution parameter data such as nitrogen dioxide (NO_2), carbon monoxide (CO), and ozone (O_3) are available starting from the middle of 2018. The vertical column density (mol/m^2) is the physical quantity or air pollution unit. Temporal analysis for changes in air pollution is the same as for data acquisition of Terra-MODIS LST imagery.

2.2.5. ERA5-land reanalysis data

Satellite-based meteorological data were used in this study. ERA5-land reanalysis (monthly) image produced by the European Center for Medium-range Weather Forecasts (ECMWF) under the auspices of the Copernicus Climate Change Service. The parameters eastward-northward components of wind speed and air temperature with a spatial resolution of $0.1^\circ \times 0.1^\circ$ are used in this study. Local and regional meteorological conditions can affect air pollution concentration in the atmosphere (Kanniah et al., 2020). Data acquired from the Google Earth Engine platform (Google Earth Engine, 2012).

2.3. Methodology

2.3.1. Spatial downscaling land surface temperature using random Forest regression

Random Forest Regression (RFR) is an ensemble machine learning technique for non-linear statistical analysis between variables consisting of multiple regression trees. The dependent variables and predictors become input data for the construction of the RFR model. Each tree is given a random sample of observations by replacing the observation values on the training data (i.e., bootstrap sampling technique) to increase the homogeneity between the features of each sub-node (Breiman, 2001). The prediction results of each trained tree are then calculated on average with the entire tree to predict the target data. This is an advantage for the RFR model because it can control high-dimensional data (Breiman, 2001). In other words, it can minimize the variance between variables. In addition, implementing the RFR model for LST downscaling needs; in fact, it is better than other regression models in terms of algorithm complexity and minimal sensitivity to multicollinearity resulting in quite a good accuracy (Li et al., 2019). In addition, it can model well even in heterogeneous landscape areas (R. Wang et al., 2020a).

Spatial downscaling LST starts from the Terra-MODIS LST image, which has a coarse-resolution converted to a finer-resolution. We set two main hyper-parameters in the RFR model, i.e., the number of variables randomly sampled as candidates at each split (mtry) by five and the number of trees (ntree) by 1000. Setting ntree of at least ~1000 can improve the performance and accuracy model, but it is not recommended to add too many trees (Li et al., 2013; Probst et al., 2019). The ratio of sharing the dataset for training and validation is 8:2. LST is more optimal through many factors, including solar radiation, topography, land cover, wind, and soil moisture (Hengl et al., 2012; Yang et al., 2019). However, we used multispectral band variables, spectral indices, and terrain factors to consider data availability in the study area. The LST spatial downscaling process in detail refers to several previous works of literature that also use the RFR model (Bartkowiak et al., 2019; W. Li et al., 2019; R. Wang et al., 2020a) include (1) spatial resolution upscaling transformation on predictor variables following the Terra-MODIS image, (2) running LST prediction process on coarse-resolution variables to obtain non-linear regression models trained for the downscaling process, (3) obtaining residual values as an error model which is then re-gridding the pixel resolution following the finer-resolution using the spline interpolation technique, and (4) LST downscaling by allocating the finer-resolution predictor variable into the RFR model that has been trained previously and substituting the error model. Overall, the spatial downscaling process were implemented in ArcGIS Pro software version 2.5 (ESRI Inc, 2020) for pre-processing LST data along with independent variables and mapping downscaled LST; then, software R-studio version 1.3.1093 (R Core Team, 2021; RStudio Team, 2020) for the spatial downscaling process.

2.3.2. Surface Urban heat intensity analysis

Surface urban heat island intensity (SUHII) provides micro-climate zone information regarding the LST differences between urban and rural zones. The SUHII calculation is described as follows (Estoque and Murayama, 2017):

$$SUHII = LST_{UZ} - mean\ LST_{RZ} \quad (1)$$

where, LST_{UZ} is the LST value of the entire pixel-based area and *mean* LST_{RZ} is the average value of the surrounding green space in the study area. We also present an analysis of the SUHII profile based on the integration of the buffer zoning method from the city center at 500-m intervals (Zhao et al., 2017) and Euclidean direction based on compass direction (i.e., North, 337.5–360° & 0–22.5°; North-west, 292.5–337.5°; West, 247.5–292.5°; South-west, 202.5–247.5°; South, 157.5–202.5°; South-east, 112.5–157.5°; East, 67.5–112.5° and North-east, 22.5–67.5°).

2.3.3. Raster re-gridding for satellite-based air pollution

The satellite-based pollutant gas dataset is a grid of pixels highlighted at a city scale. The spatial configuration of pollutant gases is naturally more subtle such as ambient air temperature, because it is related to air movement. Raster re-gridding is implemented for smoothness and continuity purposes. We use a surface interpolation approach to achieve this goal. Splines distinguish between phenomenal surfaces with smooth curves and sharp edges between the measured samples (Simpson and Wu, 2014). Spline interpolation is more suitable for applying based on the shape of the sample distribution, and the phenomena studied. Previous works of literature have also applied this technique to map ambient air pollution through ArcGIS software with good visualization results (Fang and Lu, 2011; Gharagozlou et al., 2014; Mirsanjari et al., 2020). The spatial resolution output follows the downscaled Land Surface Temperature. The type of spline used is tension with the calculation of the first derivative (slope) and the second derivative (rate of change in slope), which makes the surface smoother although increasing the computational load (Childs, 2004). The raster re-gridding process uses ArcGIS Pro software version 2.5 and spatio-temporal air pollution mapping.

2.3.4. Anomaly detection for land surface temperature and air pollution

We investigated short-term anomalies in LST and air pollution by conducting a comparative analysis between the baseline year (i.e.,

2019) and COVID-19 year (i.e., 2020), as done by several previous studies (Naqvi et al., 2021; Shikwambana et al., 2021; Singh and Chauhan, 2020a). This analysis implies the possible impact of the pandemic on reductions in heat production and gas emissions identified at initial outbreak entry (particularly in the study area), restriction stage (i.e., semi-lockdown), and easing of restrictions compared to 2019 based on meteorological conditions that are assumed to be similar. In addition, this comparative analysis aims to determine the pattern of changes in each period (before LSSR, during LSSR, and after LSSR), which shows the same or different pattern of changes. We also performed statistical analysis with a 95% confidence interval to determine whether the changes were significant or insignificant. We implemented the independent *t*-test for the difference test between the baseline year and COVID-19 year before LSSR, during LSSR, and after LSSR, respectively. Then, a Pearson correlation was carried out to determine the correlation between SUHII change (temporal change between COVID-19 year and baseline year) and air pollution (NO_2, CO, and O_3). Point samples were created using the 100 m × 100 m fishnet tool from ArcGIS (grid-based sampling) in order to retrieve pixel values from the downscaled LST, SUHII, NO_2, CO, and O_3 raster data. The methodology flow for this study can be seen in Fig. 2.

Table 3
Random Forest variable importance scores averaged across all period (2019 and 2020) in Malang City and Surabaya City.

Malang		Surabaya	
Elevation	0.653	B3	0.456
B7	0.614	B2	0.436
B8	0.581	NDBI	0.430
B2	0.576	B12	0.403
B8A	0.556	NDVI	0.402
B5	0.533	BSI	0.393
NDVI	0.483	NDWI	0.355
B3	0.479	B5	0.342
B12	0.452	B6	0.338
NDWI	0.439	B4	0.334
B4	0.423	B8A	0.310
NDBI	0.421	B11	0.293
B6	0.413	Elevation	0.282
B11	0.400	B8	0.273
BSI	0.399	B7	0.221

3. Results

3.1. Variable importance for selected predictor variables

Table 3 shows the variable importance of the predictors calculated

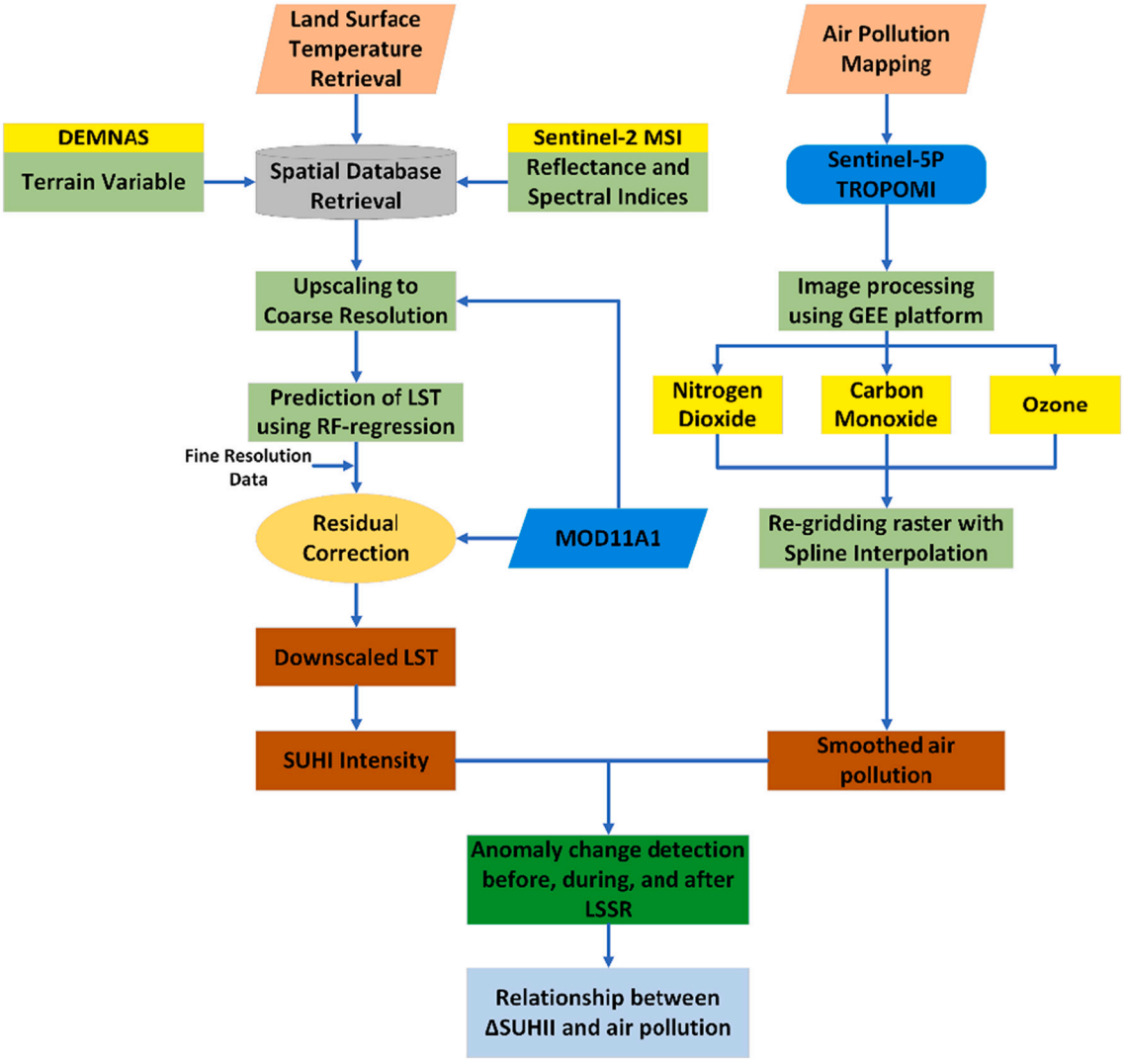

Fig. 2. Research workflow for mapping LST, SUHII, and air pollution starting from taking spatial data, spatial downscaling LST, calculating SUHII, re-gridding air pollution images, and detecting anomalies between COVID-19 year (2020) and baseline year (2019).

by the RFR model in the two study areas. The importance score represents the mean squared error (MSE). A high MSE value indicates the predictor variable is more important for the input data in the model. This importance score provides a relative rank on the contribution of the predictor variable. In fact, the ranking of variable contributions looks different in the two study areas (Table 3). Overall, the importance scores of various variables were relatively balanced in each of the two cities. The distribution of LST in Malang City is more controlled by topography and vegetation factors, such as red edge 3, NIR, red edge 4, red edge 1, and NDVI bands. These findings lead to varied vegetation and morphology, such as the presence of hills in the southeast and urban areas with slightly undulating surface relief. For the study area of Surabaya City, the complex urban landscape characteristics and relatively sloping morphology cause the elevation factor to be less important than Malang City. In addition, the blue, green, SWIR2, and all spectral indices play an important role in LST downscaling in Surabaya City. This may be due to the complex characteristics of the urban landscape, such as the presence of salt and fish ponds, urban geometry, agricultural wetlands, mangroves, and marine areas. The complexity of land cover types can trigger mixed pixels problems, and sloping morphology can reduce the importance score for the elevation factor (Wu and Li, 2019).

3.2. Downscaled land surface temperature result by random Forest regression model

The Land Surface Temperature (LST) downscaling process is beneficial for tropical climates because it is prone to cloud contamination. Downscaled LST was validated based on the root-mean-square error (RMSE), mean absolute error (MAE), and coefficient of determination (R^2). In Table 4, the average RMSE value in Surabaya is around ~1 °C, and Malang is lower, i.e., ~0.6 °C. Meanwhile, the MAE in both cities was lower than ~1 °C. Likewise, the proportion of variations in downscaled LST results is categorized as very good in both cities. Overall, the accuracy of the downscaled LST model in Surabaya is lower than that of Malang. The Random forest Regression model can also perform spatial downscaling with high accuracy.

Spatial variations probably cause a different result of accuracy between Surabaya and Malang. Land cover in Surabaya is more complex than in Malang, i.e., the type of impervious surface and vegetation is more varied, and the presence of fish ponds and salt ponds causes mixed pixels to appear. Other factors such as surface fluxes, emissivity, anisotropic, and non-linear issues can affect the model prediction (Yang et al., 2019). Apart from several issues of the spatial model, this study yielded satisfactory and robust results for microclimate studies.

3.3. Land surface temperature and surface urban heat Island intensity analysis

Comparatively, there was a decrease in Land Surface Temperature (LST) for COVID-19 against the reference year in both cities, especially during LSSR phase and after the LSSR (see Table 5). A decreased LST slightly when the LSSR was implemented by around 0.2 °C; however, some areas are showing a decline. The exception is that before the LSSR in Malang, it turned out that the LST increased by about 0.9 °C, as shown in Fig. 3. Meanwhile, the lowest LST decline was in 2020 compared to 2019, especially after the LSSR in the entire Malang City area.

Land cover in the southeast of Malang City is dryland agriculture, mixed gardens, paddy fields, and sub-urban areas (Fig. 1). In addition, LST classes with symbols in red are dominated by residential areas and slightly bare soil. Settlements in the western region and several other areas have increased LST during LSSR (i.e., 0–2 °C). Meanwhile, after the LSSR, the entire region experienced a substantial decline. The LST profile shows that Malang City forms a dome which indicates the presence of waste heat accumulated in the urban area (Fig. 4a). The buffer zone that approaches the city center is described as a valley profile that reflects the presence of urban green space in all directions (i.e., northwest-southeast, south-north, southwest-northeast, and west-east). Generally speaking, there are no apparent LST profile anomalies between the periods. Meanwhile, LST anomaly in Malang City in each period was statistically significant.

The Surabaya City area from before to after LSSR seems to experience a decrease in LST successively compared to the reference year (see Table 5). When LSSR experienced a decrease in LST by about 0.7 °C, higher than Malang City, the northwestern tip of the region is characterized by land use for salt ponds and industrial estates. Meanwhile, the east-southeast area is a mixture of fish ponds with mangroves, so it has a lower temperature than the impervious surface. In addition, aquaculture depends on the cultivation period, which allows for changes in the reflectance band so that the LST value tends to fluctuate (Ardiyansyah et al., 2021).

Spatially, the gradual decline in LST is widespread in Surabaya from before LSSR to after LSSR (Fig. 5). High-density housing, industrial estates, commercial areas, and ports experienced an even decrease in LST during LSSR and after LSSR. Meanwhile, the city of Surabaya forms a flat LST profile so that it does not form a central heat island but an even distribution of urban heat (Fig. 4b). Specifically, it reflects the dominance of built-up land, especially in the west, southwest, and south directions. Meanwhile, the highly volatile LST profile indicates the existence of mixed land uses between impervious surfaces, green spaces, and water bodies (i.e., in north, east, southeast, and northwest). In addition, we found that the LST anomaly in Surabaya City for all periods was statistically significant.

Overall, SUHII in the two cities did not appear in extreme gaps to the reference year (Figs. 6 and 7), except in the reference period before LSSR in Surabaya City, two spots appeared to the south of the city center with negative SUHI (i.e., ~2 °C). This finding may be due to the contamination factor of thin clouds that accumulated in the MODIS image mosaic during that period, resulting in low settlement temperatures. Furthermore, in 2020 there was a fluctuating change in SUHII in both cities, although not significant. Spatially and comparatively, the distribution of SUHII in the two cities varies. SUHII Malang City during LSSR period and after LSSR was slightly higher and spread westward compared to the reference year. Likewise, in Surabaya City, some locations are slightly higher than the baseline year. However, overall, it did not show a significant change in SUHII in both cities.

Table 4
Evaluation results for downscaled LST in both cities based on RMSE, MSE, and R^2, respectively.

		Surabaya			Malang		
		RMSE	MAE	R^2	RMSE	MAE	R^2
2019	Before LSSR	1.33	0.99	0.72	0.54	0.43	0.94
	During LSSR	1.04	0.78	0.83	0.61	0.48	0.92
	After LSSR	0.9	0.68	0.74	0.62	0.47	0.93
2020	Before LSSR	1.24	0.88	0.77	0.64	0.49	0.92
	During LSSR	1.11	0.84	0.82	0.72	0.52	0.89
	After LSSR	0.93	0.68	0.82	0.58	0.47	0.93

Table 5
LST anomaly between COVID-19 year and baseline year, calculated based on the average pixel value in Malang City and Surabaya City, respectively. Overall, LST anomalies in both cities were statistically significant ($P < 0.05$).

Period	Malang			Surabaya		
	2019	2020	diff (°C)	2019	2020	diff (°C)
Before LSSR	31.3	32.2	0.9	33.7	33.1	−0.6
During LSSR	31.4	31.2	−0.2	34.1	33.4	−0.7
After LSSR	31.2	29.9	−1.3	33.9	32.7	−1.2

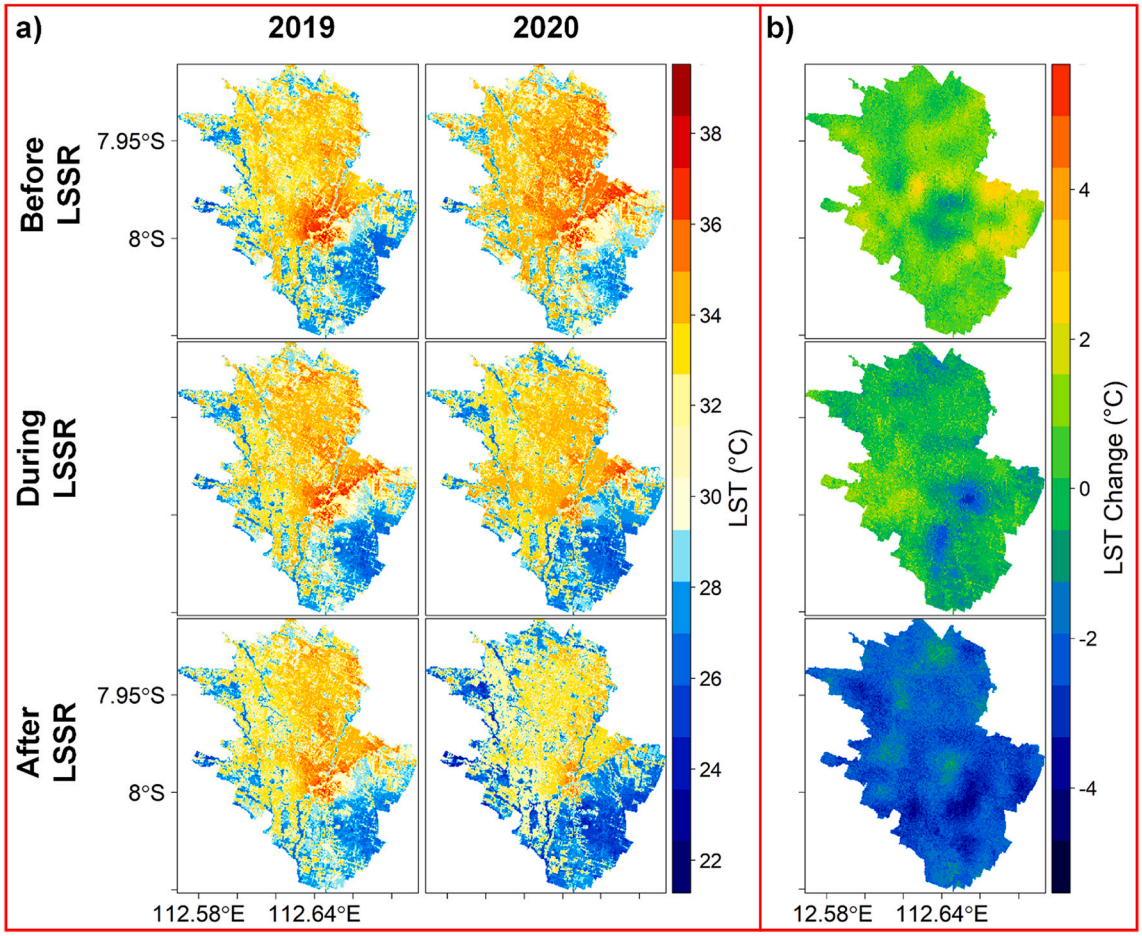

Fig. 3. a) LST map in Malang City before LSSR, during LSSR, and after LSSR; b) LST changes between the baseline year (first column) and COVID-19 year (second column). The LST classification is represented by color gradations from dark blue, yellow to dark red (representing minimum to a maximum temperature, respectively). A gradual and widespread decline in LST (third column) was detected (from before LSSR to after LSSR) in all cities represented by light blue. (For interpretation of the references to color in this figure legend, the reader is referred to the web version of this article.)

3.4. Satellite-based spatiotemporal nitrogen dioxide, carbon monoxide, and ozone patterns

Air pollution data are presented and discussed before, during, and after the partial lockdown or LSSR and compared with the baseline year. The TROPOMI S5—P satellite data is initially presented in low-resolution pixels. However, after re-gridding the raster using the spline interpolation technique, the results showed spatial variability in the concentration of pollutant gases (Figs. 8 and 9). The spline interpolation technique generally works well on air quality variable data with sparse data density (Londoño-Ciro and Cañón-Barriga, 2015). In this study, the density of input points as far as ~1-km spread out regularly over the two cities. When interpolated, a soft surface can predict the absence of gas pollutant value.

As shown in Tables 6 and 7, before LSSR phase, NO_2 in Malang City increased by around 11.4%, and Surabaya City reduced by −0.07% compared with the reference year. This study detected a substantial reduction in NO_2 in LSSR phase of around −37.82% in Malang City and − 28.42% in Surabaya City. Partial lockdown regulations (i.e., LSSR for this study) and strict lockdowns have a real impact on reducing tropospheric NO_2 gas visually through a remote sensing approach. Then, after LSSR phase showed <10% decrease in both cities, respectively. However, NO_2 increased almost twice from LSSR phase compared to the baseline year. Meanwhile, the NO_2 anomaly in both cities was statistically significant for the entire period.

The decrease in the total column density of NO_2 in the two cities could be caused by decreased vehicle emissions associated with restricting the number of vehicles allowed to move. According to Google Mobility data, it also shows a substantial decline during LSSR phase in the retail and recreation sector and transit stations, around ~30% and 55% of the baseline, respectively (Google, 2020). Industrial operations are still being carried out to maintain economic stability by implementing shift work rules and strict health protocols. This is indicated by a rather high concentration of NO_2, especially in the eastern part of Surabaya. This issue is also associated with mobility reports in the workplace sector which have decreased by ~30% from the baseline but are highly volatile from time to time. Then, the spread of NO_2 occurred during LSSR phase with a higher intensity than in the phase after LSSR. This happens because of easing of restrictions and population mobility, but health protocols are still being implemented.

Carbon monoxide (CO) is an atmospheric trace gas that comes from burning fossil fuels, burning biomass, atmospheric oxidation of methane, and other hydrocarbons (Zhao et al., 2012). The spatiotemporal CO map taken from TROPOMI is presented in Fig. 9 it shows that the CO column density changes differed from that of tropospheric NO_2 in the two cities. This happened before the LSSR phase did not experience substantial changes in both cities compared to the reference year. Even in LSSR phase and after, there was an increase in CO in both cities, but not >10% (Tables 6 and 7). This may be influenced by the atmospheric lifetime factor, which is longer than NO_2, so the emission changes are not so significant at the local scale (Elshorbany et al., 2021). Also, it is less sensitive to short-term anthropogenic emission changes.

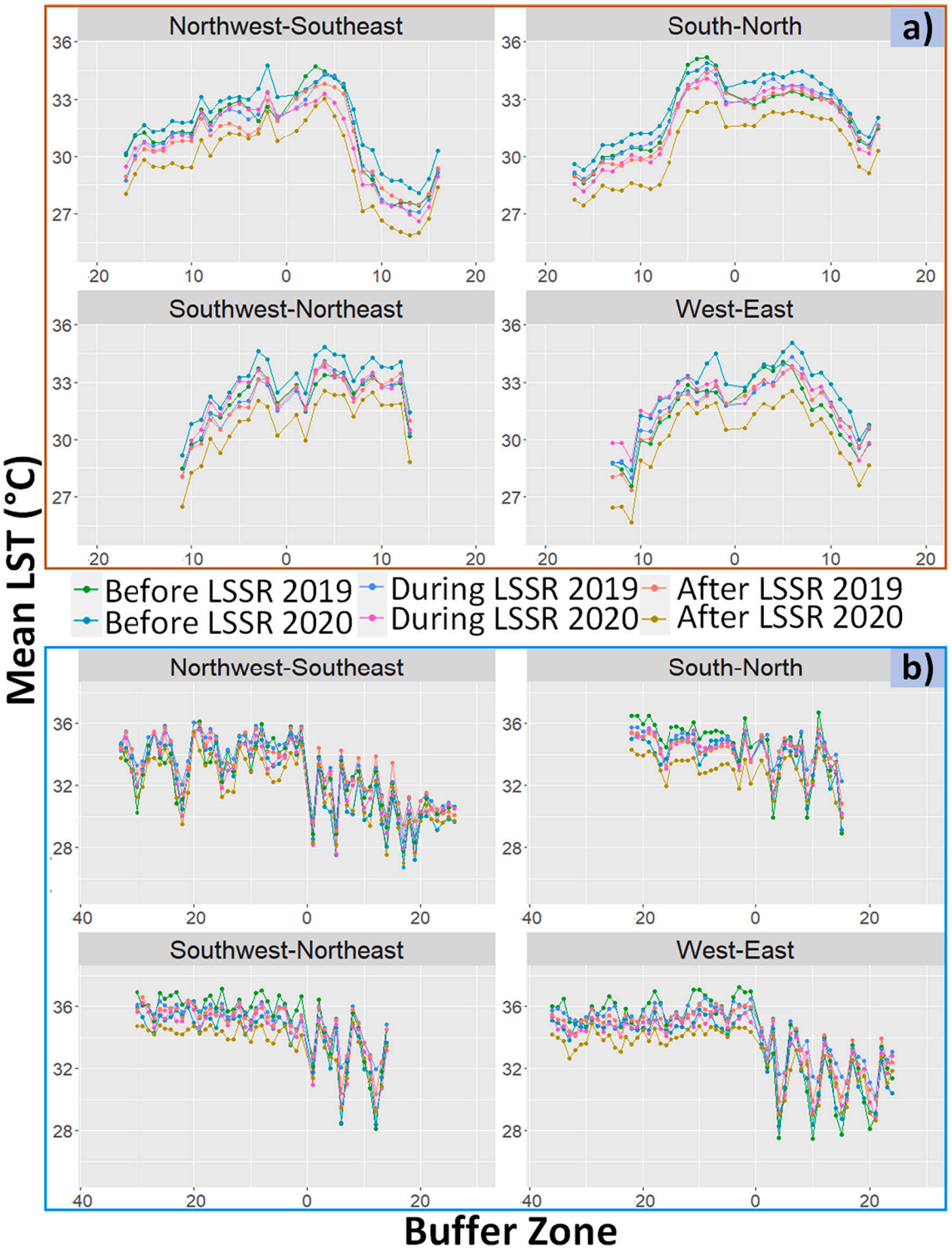

Fig. 4. LST profile-based in a) Malang City and b) Surabaya City. The LST profile is plotted based on the average pixel value of the buffer and euclidean direction overlaid zones with the LST map.

However, the overall change in CO column density was statistically significant, but the value is small. The spatio-temporal diffusion of the CO column density in both cities looks uneven. CO gas spreads randomly over time, unlike NO_2, which spatially has a clear agglomeration pattern in both cities.

Overall, ozone gas (O_3) decreased slightly in both cities compared to the baseline year. The distribution pattern of O_3 gas shows spatial variations that tend to be homogeneous in both cities (Fig. 10), i.e., before, during, and after LSSR. Furthermore, during LSSR phase, it was reduced by ~4% in both cities (Tables 6 and 7). However, the O_3 anomaly was statistically significant in both cities. This indicates that natural processes cause the ozone anomaly in the study area without the intervention of anthropogenic emissions. In addition, the slight decrease in O_3 gas during the LSSR phase may be due to meteorological conditions.

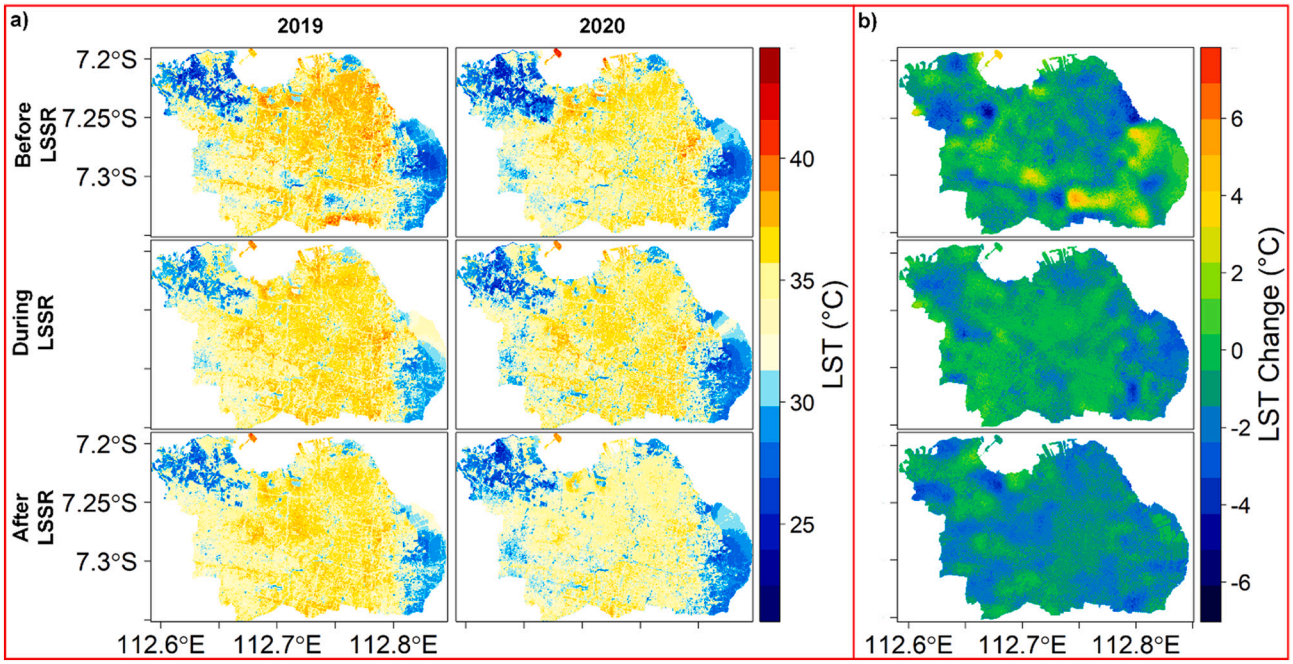

Fig. 5. (a) LST map in Surabaya City before LSSR, during LSSR, and after LSSR; (b) changes in LST between the baseline year (first column) and the COVID-19 year (second column). The LST classification is represented by color gradations from dark blue, yellow to dark red (representing minimum to a maximum temperature, respectively). A gradual and widespread decrease in LST (third column) was detected (from before LSSR to after LSSR) in entire cities represented in blue. (For interpretation of the references to color in this figure legend, the reader is referred to the web version of this article.)

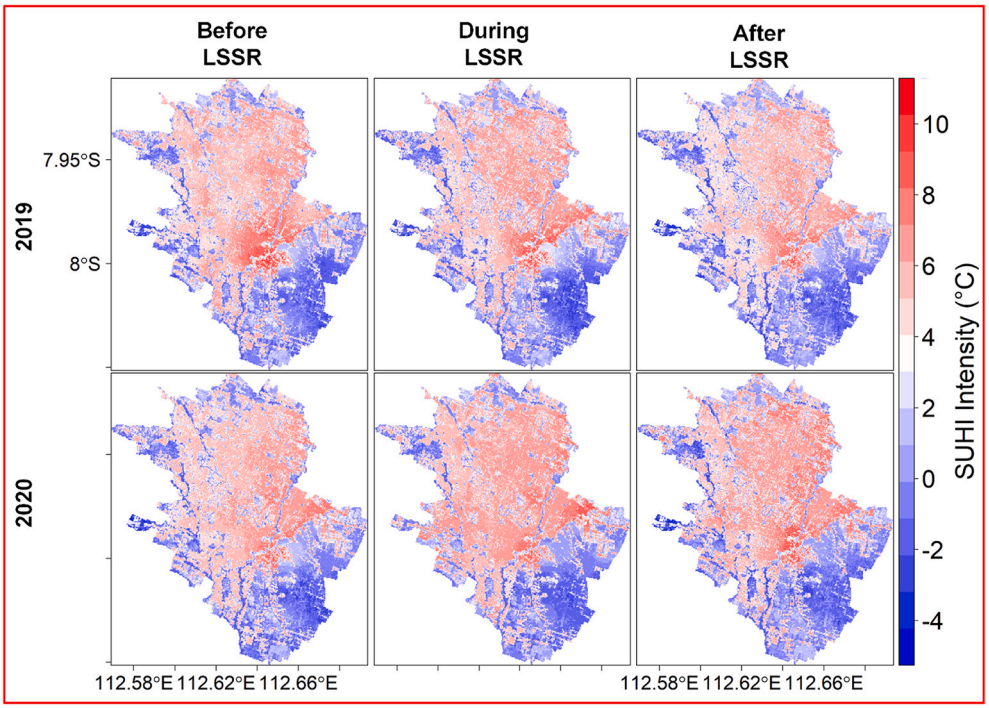

Fig. 6. SUHII map in Malang City in the period before LSSR, during LSSR, and after LSSR in the baseline year in 2019 (first row), and COVID-19 year in, 2020 (second row). Red color indicates high intensity; blue color indicates low intensity. (For interpretation of the references to color in this figure legend, the reader is referred to the web version of this article.)

3.5. Relationship between SUHII change, air temperature, and wind speed with the air pollution in both cities

The correlation analysis of SUHII change (ΔSUHII) versus air pollution (NO_2, CO, and O_3) in Surabaya City and Malang City is shown in Table 8. Statistically, the correlation between ΔSUHII and air pollution in both cities was significant ($P < 0.05$). It is clear that there is a positive correlation between ΔSUHII with NO_2 and CO in both cities when LSSR was implemented. Malang City has a slightly higher ΔSUHII-NO_2 correlation ($r = 0.33$) than Surabaya City ($r = 0.14$) during LSSR

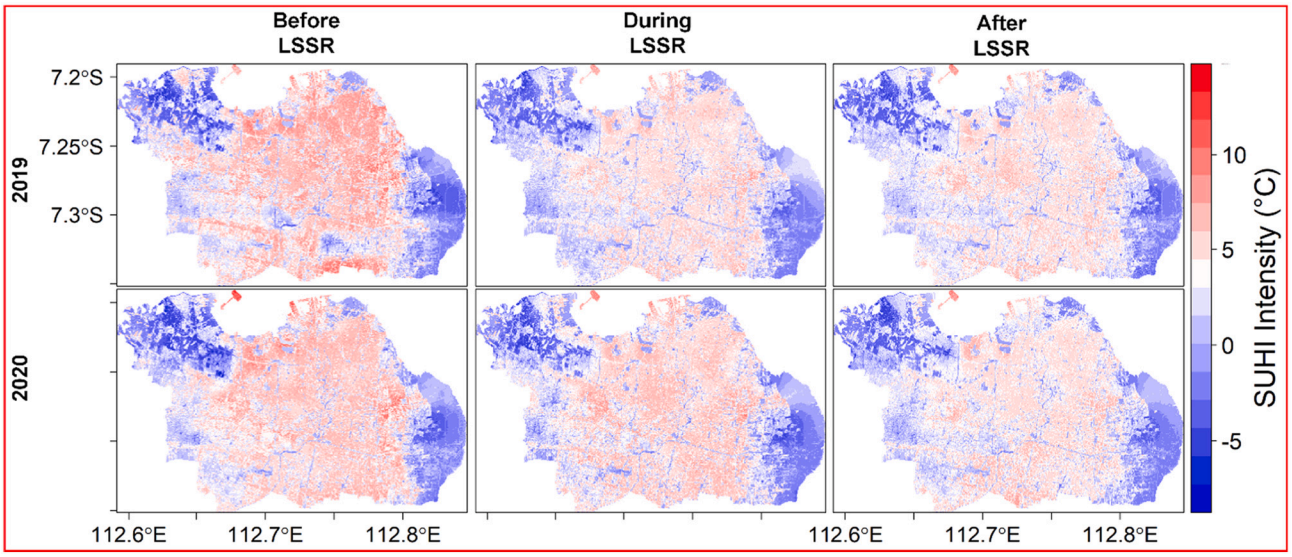

Fig. 7. SUHII map in Surabaya City in the period before LSSR, during LSSR, and after LSSR in the baseline year in 2019 (first row), and COVID-19 year in 2020 (second row). Red color indicates high intensity; blue color indicates low intensity. (For interpretation of the references to color in this figure legend, the reader is referred to the web version of this article.)

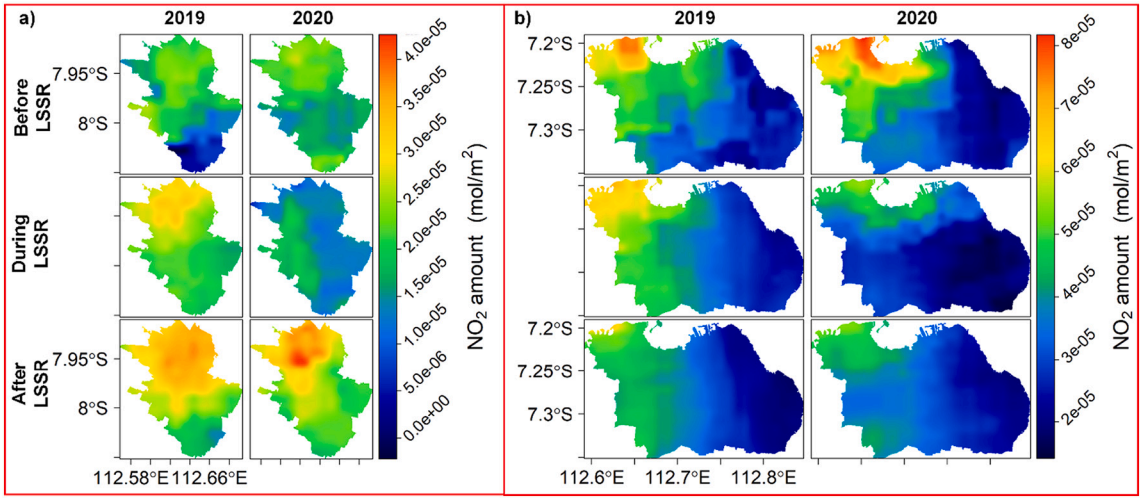

Fig. 8. NO_2 map in (a) Malang City and (b) Surabaya City in the period before LSSR, during LSSR, and after LSSR with comparing the baseline year of 2019 and COVID-19 year of 2020. Both cities show a pattern of changes in the distribution of nitrogen emission gases dioxide compared to the baseline year. The concentration of nitrogen dioxide gas in the satellite-based atmosphere is measured in units of mols per squared meter. Dark blue color indicates the lowest emission, followed by blue, green, yellow, orange to red color gradations indicating the presence of higher emissions. (For interpretation of the references to color in this figure legend, the reader is referred to the web version of this article.)

phase. A positive correlation was also seen in both cities during the easing of restrictions. On the other hand, the phase before LSSR showed a negative correlation in Malang City ($r = -0.16$) and Surabaya City ($r = -0.13$).

Meanwhile, the correlation of ΔSUHII-CO in Surabaya City ($r = 0.29$) was slightly higher than Malang City ($r = 0.19$) during LSSR. However, the correlation in both cities is very low after LSSR, which is almost zero. In addition, the negative correlation of this pollutant gas in the second before LSSR. For O_3 gas, all periods in both cities have a negative correlation with ΔSUHII, except for Surabaya, which has a positive correlation but is very low in the period before LSSR. At the time of LSSR, the City of Surabaya showed the largest negative correlation between ΔSUHII-O_3, among others. However, there is an inconsistency in the correlation of ΔSUHII with pollutant gases between periods in both cities, such as NO_2 and CO which are negatively correlated in before LSSR, but during LSSR is positively correlated. From this, indicates that NO_2 are directly related to the amount of pollutants released from anthropogenic activities, especially vehicle and industrial emissions. The intensity of solar radiation touches the earth's surface more so that SUHII increases (Kalisa et al., 2018) because the amount of NO_2 concentration is less. However, it is necessary to study further this relationship with the intensity of solar radiation. In addition, CO gas showed a positive correlation with ΔSUHII but experienced a slight increase, as discussed in section 3.4. Likewise, with O_3 gas, where there is no extreme anomaly during LSSR, especially for negative correlation in Surabaya City ($r = -0.28$). However, the correlation of ΔSUHII with the three pollutant gases is low.

Concerning the anomaly pattern of air pollution, ERA5-Land imagery reanalysis of monthly averages (i.e., before LSSR, during LSSR, and after LSSR in baseline year and COVID-19 year) is presented to determine the effect of air temperature and wind speed with anomalies pollutant gases in both cities. However, this is indicated as it is limited to the spatial

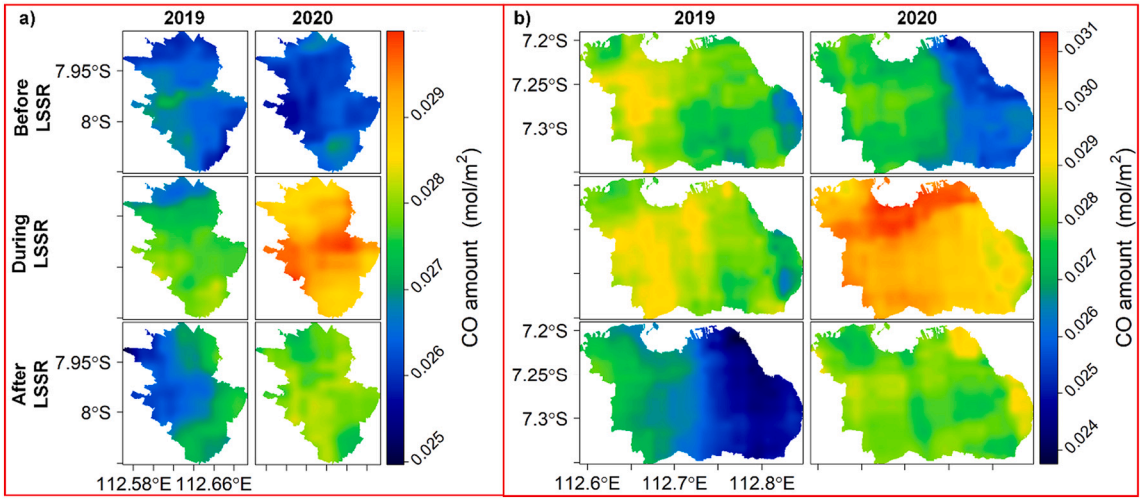

Fig. 9. Same as Fig. 8, but for carbon monoxide. The map color symbol for carbon monoxide is the same as for nitrogen dioxide and uses mols per squared meters as the unit of quantity. Both cities show spatially varying changes in carbon monoxide.

Table 6
Mean difference in NO_2, CO, and O_3 between the COVID-19 year and baseline year is calculated based on the average pixel value in Malang City. Overall, the air pollution anomaly in Malang City was statistically significant ($P < 0.05$).

Period	NO_2 (mol/m^2)			CO (mol/m^2)			O_3 (mol/m^2)		
	2019	2020	diff (%)	2019	2020	diff (%)	2019	2020	diff (%)
Before LSSR	1.73E-05	1.92E-05	11.40%	0.0265	0.0262	−1.01%	0.11547	0.11281	−2.30%
During LSSR	2.38E-05	1.48E-05	−37.82%	0.0275	0.0291	5.73%	0.11545	0.11049	−4.29%
After LSSR	2.85E-05	2.69E-05	−5.79%	0.0268	0.0279	4.10%	0.11355	0.11043	−2.75%

Table 7
Mean difference in NO_2, CO, and O_3 between the COVID-19 year and baseline year is calculated based on the average pixel value in Surabaya City. Overall, the air pollution anomaly in Surabaya City was statistically significant ($P < 0.05$).

Period	NO_2 (mol/m^2)			CO (mol/m^2)			O_3 (mol/m^2)		
	2019	2020	diff (%)	2019	2020	diff (%)	2019	2020	diff (%)
Before LSSR	3.84E-05	3.84E-05	−0.07%	0.0280	0.0269	−3.99%	0.11676	0.11386	−2.49%
During LSSR	3.94E-05	2.82E-05	−28.42%	0.0284	0.0299	5.42%	0.11674	0.11146	−4.52%
After LSSR	3.39E-05	3.27E-05	−3.47%	0.0259	0.0281	8.31%	0.11456	0.11153	−2.64%

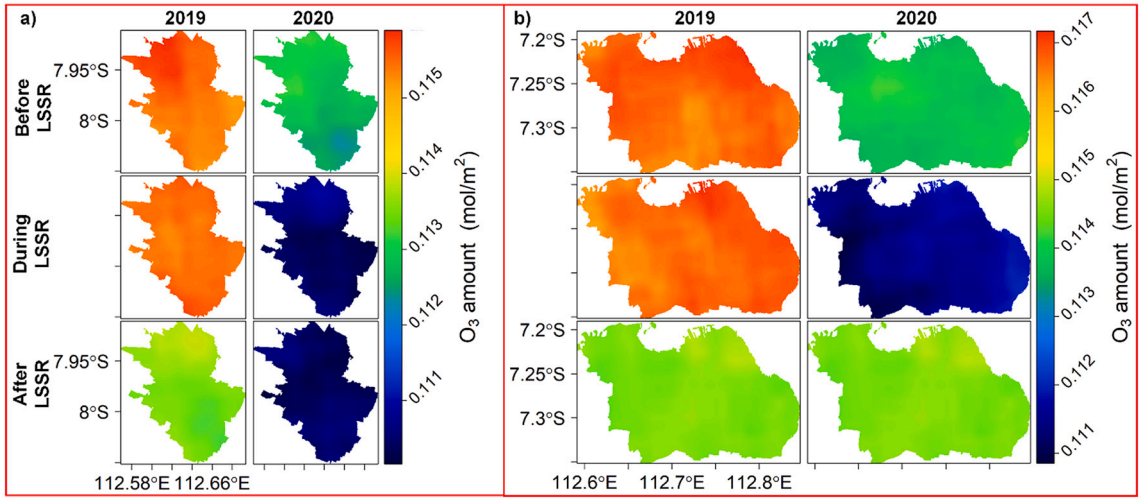

Fig. 10. Same as Fig. 8, but for ozone. The color symbol for the ozone map is the same as for nitrogen dioxide and carbon monoxide and uses mols per squared meter as the unit of quantity. On the map, changes in ozone gas tend to be spatially homogeneous in both cities.

Table 8
Correlation between SUHII changes and air pollution conditions in the COVID-19 year period before LSSR, during LSSR, and after LSSR.

Period	ΔSUHII-NO_2		ΔSUHII-CO		ΔSUHII-O_3	
	Malang	Surabaya	Malang	Surabaya	Malang	Surabaya
Before LSSR	r = −0.16, P < 0.05	r = −0.13, P < 0.05	r = −0.14, P < 0.05	r = −0.05, P < 0.05	r = −0.04, P < 0.05	r = 0.07, P < 0.05
During LSSR	r = 0.33, P < 0.05	r = 0.14, P < 0.05	r = 0.19, P < 0.05	r = 0.29, P < 0.05	r = −0.07, P < 0.05	r = −0.28, P < 0.05
After LSSR	r = 0.20, P < 0.05	r = 0.11, P < 0.05	r = 0.04, P < 0.05	r = −0.09, P < 0.05	r = −0.15, P < 0.05	r = −0.06, P < 0.05

Table 9
Monthly average ERA5-land air temperature levels (in degrees Celsius) in Malang City and Surabaya City for 2019 and 2020 in the period before LSSR, during LSSR, and after LSSR. A total of four pixels for Malang City and three for Surabaya City were made for the analysis of the mean, standard deviation, and differences.

Period	Malang (4 pixels)			Surabaya (3 pixels)		
	2019	2020	diff (°C)	2019	2020	diff (°C)
Before LSSR	24.45 ± 0.31	24.70 ± 0.46	+0.25	26.84 ± 0.10	27.00 ± 0.12	+0.16
During LSSR	23.90 ± 0.02	24.60 ± 0.32	+0.70	27.41 ± 0.005	27.59 ± 0.01	+0.18
After LSSR	22.76 ± 0.01	23.30 ± 0.20	+0.54	27.19 ± 0.03	27.20 ± 0.11	+0.01

Table 10
Monthly average ERA5-land wind speed levels (in m/s) and wind direction in Malang City and Surabaya City for 2019 and 2020 before LSSR, during LSSR, and after LSSR. A total of four pixels for Malang City and three for Surabaya City were made for the analysis of the mean, standard deviation, and difference.

Period	Malang (4 pixels)			Surabaya (3 pixels)		
	2019	2020	diff (%)	2019	2020	diff (%)
Before LSSR	0.55 ± 0.21	0.47 ± 0.18	−15	0.65 ± 0.007	0.70 ± 0.01	+3
During LSSR	1.23 ± 0.40	0.68 ± 0.29	−45	0.99 ± 0.09	1.10 ± 0.11	+10
After LSSR	1.30 ± 0.38	1.30 ± 0.46	0	1.29 ± 0.09	1.10 ± 0.10	−15

resolution spanning a regional scale (~11-km). As shown in Fig. 11, the spatial variation is limited, so statistical analysis of the relationship cannot be carried out. Specifically, a simple numerical analysis is carried out, which is indicated by area-of-interest (black boxes) on the map.

Tables 9 and 10 show a descriptive analysis of the air temperature and wind speed, which calculated the average value and standard deviation for each period in the baseline year and COVID-19 year. Overall, there was a slight increase in air temperature in both cities (i.e., between 2019 and 2020). The temperature increases the highest in Malang during LSSR (+0.7 °C) compared to before LSSR (+0.25 °C) and after LSSR (+0.54 °C). Meanwhile, changes in air temperature tend to be stable in each period in Surabaya City (~0.1 °C).

In addition, CO and O_3 gases tend to stabilize during a pandemic; however, a slight increase/decrease can be attributed to the dispersion of pollutants from other cities by the wind. However, as shown in Fig. 11, winds moving from the south-west direction allow transport of pollutants from other locations. In fact, wind speed varied in both cities in each period (Table 10). In Malang City, the difference in wind speed in the period before LSSR (−15%) and after LSSR (stagnant) causes NO_2 pollutant particles to accumulate in the city. Meanwhile, during LSSR (−45%) there was a significant decrease, which made it clear that the NO_2 reduction was caused by a decrease in human activities at that time. In other hand, Surabaya City indicated that the source of NO_2 pollutants

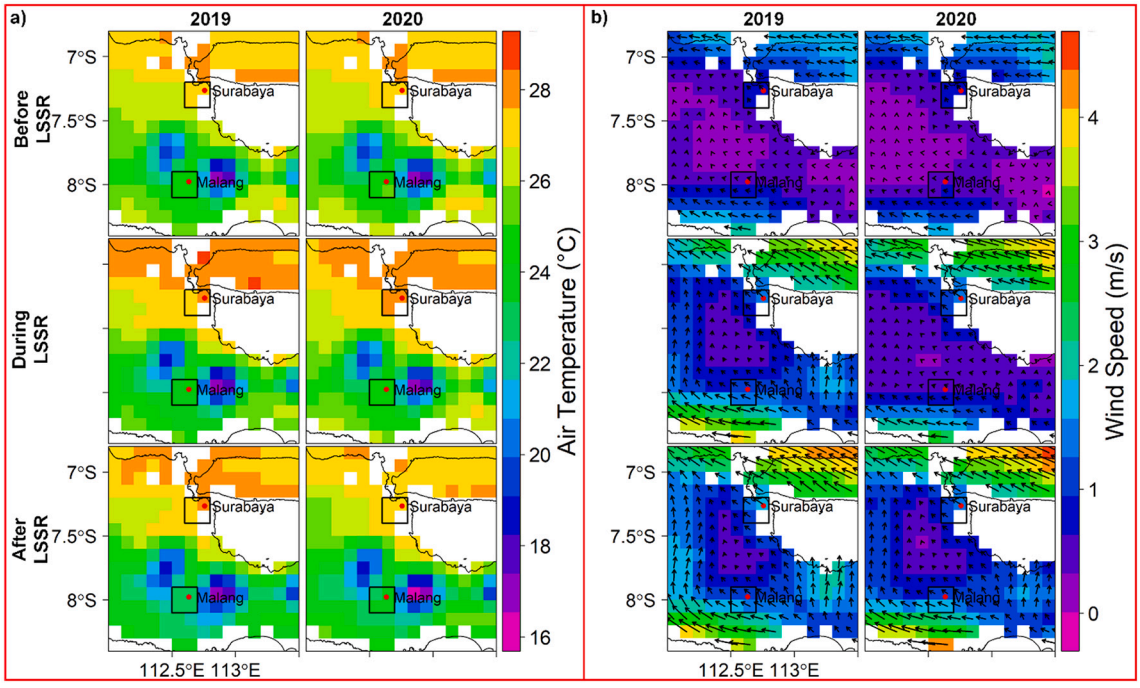

Fig. 11. (a) map of air temperature in units of degrees Celsius and (b) wind speed in units of m/s for the baseline year (first column and third column) and COVID-19 year (second column and fourth column). First row, before LSSR; second row, during LSSR; third row, after LSSR. The arrow symbol in the wind speed map indicates the direction of the wind. The square plot marks the.

came from other cities because during LSSR, the wind speed was slightly higher (1.1 m/s) than Malang City (0.68 m/s). Meanwhile, CO and O_3 gases do not seem to have anything to do with wind speed in both cities when seen from the comparison between the total concentration and wind speed for each period in 2019 and 2020 (Tables 7, 8, and 10).

4. Discussion

The LST results reported in this study showed a slight decrease during the LSSR phase compared to the baseline year. Generally speaking, decreased LST in mountainous (i.e., Malang City) and coastal cities (i.e., Surabaya City) due to limiting anthropogenic activities depends on the local climate, population density, industrial operations, agricultural, commercial, and transportation activities (Nanda et al., 2021). In fact, our study showed that the LSSR phase was not very effective in reducing LST. This finding is almost similar to the results obtained in the study of Shikwambana et al. (2021), but conversely that the LST during the lockdown period for the pandemic year (i.e., 2020) was slightly higher than the baseline year (i.e., 2019) (Shikwambana et al., 2021). However, LST changes can also be influenced by the radiation characteristics and energy absorption of land cover type (Faqe Ibrahim, 2017). Comparatively and in accordance with the LST results, the SUHI intensity during the LSSR phase was slightly lower than the baseline year. We suspect that the cause may be because LSSR does not completely stop human activities in the city, and some industries are still operating, so the reduction of the greenhouse effect is not so significant. Another possibility is more likely to be associated with seasonal effects or cooler weather factors rather than LSSR regulatory interventions.

The results reported in this study indicate a reduction in pollutants, particularly NO_2, in both cities during the LSSR phase concerning the COVID-19 pandemic situation. The reduction in NO_2 that occurs is in line with several similar studies in other cities or regions that apply activity restrictions (Nakada and Urban, 2020; Pei et al., 2020; Singh and Chauhan, 2020b). In contrast, CO gas showed a slight increase during the LSSR phase, which is in line with the results of studies in several areas such as Chicago, Houston, San Francisco, and Los Angeles in the United States (Elshorbany et al., 2021) or the northwest and southern provinces of China (Fan et al., 2020) with increased CO levels. This means reducing vehicle traffic when the LSSR phase in our study area is ineffective in reducing CO levels that other pollutant sources may cause. O_3 gas reduction also occurred in both cities during the LSSR phase. Some of the possibilities that cause O_3 reduction include cloudy weather conditions resulting in inhibition of the oxidation process so that O_3 formation is reduced, conditions of relative humidity and high ultraviolet radiation in tropical climates stimulate secondary particulate formations, which can inhibit O_3 production, tropical convection can also trigger O_3 reduction, and the effect of local meteorology also plays an important role in reducing O_3 when activity is restricted (Bouarar et al., 2021; Qiu et al., 2021; Shek et al., 2022). With respect to anthropogenic heat and pollutant emissions, it is clear that air pollution, especially NO_2 and CO, is directly correlated with SUHII in the LSSR phase, indicating that these two pollutants support the development of SUHI in both cities. On the other hand, high O_3 gas in the total column was associated with the development of low SUHI. This correlation result is in line with the study of the relationship between UHI intensity and ambient air pollution in Seoul City, that O_3 is negatively correlated with UHI intensity, while CO and NO_2 are positively correlated (Ngarambe et al., 2021). Satellite-based air temperature and wind speed observations are offered in this study. The results revealed that the variable air temperature increased in both cities during the LSSR phase, while the wind speed decreased in Malang City and slightly increased in Surabaya. Ghasempour et al. (2021) reported that air temperature strongly correlates negatively with NO_2 (Ghasempour et al., 2021). However, our findings differ from this study in that air temperature slightly increases while NO_2 concentration decreases at LSSR phase. Wind variables generally indicate the dispersion of pollutant gases at higher wind speed conditions. However, the pollutant concentration is generally inversely proportional to the wind speed; when the concentration increases, it can go downwind even at high wind speeds (Kim et al., 2004). This occurs in our study results when reduced wind speed does not necessarily cause the dispersion of pollutant gases, e.g., CO gas which increases during the LSSR phase. We expect that other meteorological factors, such as precipitation, soil moisture, relative humidity, absolute humidity, solar radiation, etc., may play an important role in changes in CO and O_3 gases in both cities.

The results of LST spatial downscaling for the study area of Surabaya City and Malang City show evidence that the RFR model works well. Similiarly, Li et al. (2019) revealed that downscaled LST using machine learning gives satisfactory results in areas of dense vegetation and impervious surfaces (Li et al., 2019). Ebrahimy and Azadbakht (2019) revealed that the RFR model shows good model stability, high accuracy, and efficient computation in LST spatial downscaling processes (Ebrahimy and Azadbakht, 2019). For non-spatial studies, Nematchoua et al. (2022) revealed that several machine learning algorithms, including RFR, produced predictive models of daily global solar radiation and air temperature in European cities in 2050 and 2100 with good accuracy. (Nematchoua et al., 2022). Experiments on several input variables offered in this study can encourage a promising LST spatial downscaling method for urban climate and epidemiological studies. In addition to investigating the effect of LSSR implementation on LST changes studied in this study, the spatial downscaling LST model can also be used as input data for ecological spatial modeling studies. Amiri et al. (2020) compared input data sources for bioclimatic variables (i.e., temperature and precipitation), which reported that remote sensing data yielded more up-to-date information and improved species distribution modeling performance than field observation data. (Amiri et al., 2020). In addition, the spatial and temporal resolution factors in remote sensing data are valuable attributes for the study of ecological systems such as phenological changes, climate change, biodiversity, and species distribution modeling. (Boyd and Foody, 2011). In this sense, our proposed LST spatial downscaling model may be able to overcome the low spatial and temporal problems for ecological spatial studies in areas with local scales.

Then, air pollution mapping in this study can indicate changes in atmospheric conditions based on remote sensing due to the LSSR phase. The interpolation technique of air pollution image data with coarse spatial resolution shows finer spatial patterns. This is one of the benefits for areas where only low-density stations are available. Bezyk et al. (2021) revealed that the thin spline interpolation technique provides a ground-based prediction of air pollution variations in the atmosphere with good accuracy; however, there are unmeasured locations (Bezyk et al., 2021). This implies that the sample locations resulting from the transformation of raster data to spatial points form local surface variations because their distribution is more uniform than ground-based locations. However, another case by Kumar et al. (2022) found that spline interpolation is not recommended for ground-based air quality mapping due to overestimation and underestimation problems resulting in negative values (Kumar et al., 2022). In addition, the spatial pattern of emissions in urban areas is very likely to be influenced by anthropogenic emission factors.

The spatial pattern of surface temperature can be explained through the spectral band, spectral index, and topography variables. However, the urban surface temperature is certainly influenced by other factors besides those carried out in this study. Therefore, more complex independent variables can be added for further research, such as the morphology of urban architecture (distribution and building structure) and road factors. In addition, feature selection analysis was required to reduce data redundancy, affecting the results of spatial downscaling. It should be noted that the importance score will change when the number of predictor variables is considered. Therefore, further studies are needed regarding uncertainty, bias, spatial variability, and reliability in spatial interpolation techniques, especially for remote sensing-based air pollution data.

5. Conclusions

This study investigates spatiotemporal changes during the COVID-19 pandemic in land surface temperature, nitrogen dioxide, carbon monoxide, and ozone in Malang City and Surabaya City based on remote sensing. A total of three periods were considered from 30th March to 27th June 2020 (before, during, and after LSSR) and compared with reference years (i.e., 2019) for comparative analysis of their changes. Spatial downscaling Land Surface Temperature using machine learning techniques, i.e., Random Forest Regression, shows satisfactory results for urban-scale micro-climate studies. The results show an LST anomaly is statistically significant in both cities, but the temperature is slightly reduced in both cities. The spatial distribution of LST anomalies in both cities before, during, and after LSSR phase is more likely to be evenly distributed. Furthermore, SUHII in both cities, particularly in LSSR phase, showed a slightly increase in intensity from the baseline year.

Establishing LSSR regulations in both cities resulted in improved air quality, particularly reducing nitrogen dioxide emissions by ~37% in Malang City and ~28% in Surabaya City. Emission reductions are caused by the effects of shifting work, restrictions on transportation and recreational sites, work and study from home, etc. However, restricted anthropogenic activities do not decrease carbon monoxide levels or increase ozone. In addition, the partial lockdown or LSSR regulations imposed in Malang City and Surabaya City tend to only reduce traffic vehicle emissions (i.e., NO_2) due to restrictions on mobilization and partial closure of public facilities, entertainment venues, work-from-home, and businesses; however, it is not effective in controlling the effect of city heat island, particularly for CO and O_3. The relationship between SUHII changes and air pollution varied in the two cities, but the degree of correlation was low. NO_2 is directly related to SUHII changes because this pollutant is released mainly from transportation and human activities. Meanwhile, there is no definite correlation between SUHII changes with CO and O_3.

Likewise, meteorological factors seem to need further study on this matter because of limited spatial resolution in the ERA5-land reanalysis image and adding other factors, e.g., rainfall, soil moisture, relative humidity, absolute humidity, solar radiation, etc. In addition, spatial interpolation techniques for remote sensing-based air pollution need to be analyzed further, especially in urban areas where observation stations are rarely located. This research is limited to the use of remotely sensed data, so it is necessary to validate the reliability of the data by conducting in-situ measurements for future work.

This study provides insight into the ecological impact of urban areas between the partial level limitation of anthropogenic activities caused by COVID-19 and changes in surface temperature, the formation of SUHI, changes in pollutant gases, and the mechanism of the relationship between changes in SUHI and air pollution gases and their meteorological parameters, i.e., air temperature and wind speed. The spatial downscaling LST model and re-gridding satellite-based air pollution offered in this study can be applied by decision-makers to develop the most efficient strategy to improve local air quality in the long and short term in the future. In addition, the current model can be applied to other ecological studies as a descriptor of an ecological spatial model with improved data quality.

Declaration of Competing Interest

The authors declare no conflict of interest.

Data availability

The data that has been used is confidential.

Acknowledgments

The study received no funding from agencies or commercials. The project was funded internally by Universitas Negeri Malang with a research grant scheme. We thank the university's research institute for providing the opportunity to conduct research on the effect of government policies on the city's microclimate environment.

References

Amiri, M., Tarkesh, M., Jafari, R., Jetschke, G., 2020. Bioclimatic variables from precipitation and temperature records vs. remote sensing-based bioclimatic variables: which side can perform better in species distribution modeling? Ecol. Inform. 57, 101060 https://doi.org/10.1016/j.ecoinf.2020.101060.

Ardiyansyah, A., Munir, A., Gabric, A., 2021. The utilization of land surface temperature information as an input for coastal city. IOP Conf. Ser.: Earth Environ. Sci. 921 (1), 012004 https://doi.org/10.1088/1755-1315/921/1/012004.

Bartkowiak, P., Castelli, M., Notarnicola, C., 2019. Downscaling land surface temperature from MODIS dataset with random Forest approach over alpine vegetated areas. Remote Sens. 11 (11), 1319. https://doi.org/10.3390/rs11111319.

Berila, A., Isufi, F., 2021. Mapping summer SUHI and its impact on the environment using GIS and remote sensing techniques: a case study on municipality of Prishtina (Kosovo). Eur. J. Geogr. 12 (3), 113–129. https://doi.org/10.48088/ejg.aber.12.3.113.129.

Berman, J.D., Ebisu, K., 2020. Changes in U.S. air pollution during the COVID-19 pandemic. Sci. Total Environ. 739, 139864 https://doi.org/10.1016/j.scitotenv.2020.139864.

Bezyk, Y., Sówka, I., Górka, M., Blachowski, J., 2021. GIS-based approach to Spatio-temporal interpolation of atmospheric CO2 concentrations in limited monitoring dataset. Atmosphere 12 (3), 384. https://doi.org/10.3390/atmos12030384.

BIG, 2008. DEMNAS. http://tides.big.go.id/DEMNAS/.

Bouarar, I., Gaubert, B., Brasseur, G.P., Steinbrecht, W., Doumbia, T., Tilmes, S., Liu, Y., Stavrakou, T., Deroubaix, A., Darras, S., Granier, C., Lacey, F., Müller, J., Shi, X., Elguindi, N., Wang, T., 2021. Ozone anomalies in the free troposphere during the COVID-19 pandemic. Geophys. Res. Lett. 48 (16) https://doi.org/10.1029/2021GL094204.

Boyd, D.S., Foody, G.M., 2011. An overview of recent remote sensing and GIS based research in ecological informatics. Ecol. Inform. 6 (1), 25–36. https://doi.org/10.1016/j.ecoinf.2010.07.007.

BPS Kota Malang, 2021. Kota Malang Dalam Angka.

BPS Kota Surabaya, 2021. Kota Surabaya Dalam Angka.

Breiman, L., 2001. Random forests. Mach. Learn. 45, 5–32.

Chavez, P., Sides, S.C., Anderson, J.A., 1991. Comparison of three different methods to merge multiresolution and multispectral data-Landsat TM and SPOT panchromatic. Photogramm. Eng. Remote. Sens. 57 (3), 295–303.

Chen, Q.-X., Huang, C.-L., Yuan, Y., Tan, H.-P., 2020. Influence of COVID-19 event on air quality and their Association in Mainland China. Aerosol Air Qual. Res. 20 (7), 1541–1551. https://doi.org/10.4209/aaqr.2020.05.0224.

Childs, C., 2004. Interpolating surfaces in ArcGIS spatial analyst. ArcUser. 7 (3), 32–35.

Cui, Y., Xu, X., Dong, J., Qin, Y., 2016. Influence of urbanization factors on surface Urban Heat Island intensity: a comparison of countries at different developmental phases. Sustainability 8 (8), 706. https://doi.org/10.3390/su8080706.

Das, R.D., Bandopadhyay, S., Das, M., Chowdhury, M., 2020. In: Global Air Quality Change Detection During Covid-19 Pandemic Using Space-Borne Remote Sensing and Global Atmospheric Reanalysis. 2020 IEEE India Geoscience and Remote Sensing Symposium (InGARSS), pp. 158–161. https://doi.org/10.1109/InGARSS48198.2020.9358918.

Desjardins, M.R., Hohl, A., Delmelle, E.M., 2020. Rapid surveillance of COVID-19 in the United States using a prospective space-time scan statistic: detecting and evaluating emerging clusters. Appl. Geogr. 118 (March), 102202 https://doi.org/10.1016/j.apgeog.2020.102202.

Duan, S.-B., Li, Z.-L., 2016. Spatial downscaling of MODIS land surface temperatures using geographically weighted regression: case study in northern China. IEEE Trans. Geosci. Remote Sens. 54 (11), 6458–6469. https://doi.org/10.1109/TGRS.2016.2585198.

Ebrahimy, H., Azadbakht, M., 2019. Downscaling MODIS land surface temperature over a heterogeneous area: an investigation of machine learning techniques, feature selection, and impacts of mixed pixels. Comput. Geosci. 124, 93–102. https://doi.org/10.1016/j.cageo.2019.01.004.

Elshorbany, Y.F., Kapper, H.C., Ziemke, J.R., Parr, S.A., 2021. The status of air quality in the United States during the COVID-19 pandemic: a remote sensing perspective. Remote Sens. 13 (3), 369. https://doi.org/10.3390/rs13030369.

ESRI Inc, 2020. ArcGIS Pro (2.5). ESRI Inc.. https://www.esri.com/en-us/arcgis/products/arcgis-pro/overview

Estoque, R.C., Murayama, Y., 2017. Monitoring surface urban heat island formation in a tropical mountain city using Landsat data (1987–2015). ISPRS J. Photogramm. Remote Sens. 133, 18–29. https://doi.org/10.1016/j.isprsjprs.2017.09.008.

Fan, C., Li, Y., Guang, J., Li, Z., Elnashar, A., Allam, M., de Leeuw, G., 2020. The impact of the control measures during the COVID-19 outbreak on air pollution in China. Remote Sens. 12 (10), 1613. https://doi.org/10.3390/rs12101613.

Fang, T.B., Lu, Y., 2011. Constructing a near real-time space-time cube to depict Urban ambient air pollution scenario. Trans. GIS 15 (5), 635–649. https://doi.org/10.1111/j.1467-9671.2011.01283.x.

Faqe Ibrahim, G., 2017. Urban land use land cover changes and their effect on land surface temperature: case study using Dohuk City in the Kurdistan region of Iraq. Climate 5 (1), 13. https://doi.org/10.3390/cli5010013.

Galvin, C.J., Li, Y.-C., Malwade, S., Syed-Abdul, S., 2020. COVID-19 preventive measures showing an unintended decline in infectious diseases in Taiwan. Int. J. Infect. Dis. 98, 18–20. https://doi.org/10.1016/j.ijid.2020.06.062.
Gao, B., 1996. NDWI—A normalized difference water index for remote sensing of vegetation liquid water from space. Remote Sens. Environ. 58 (3), 257–266. https://doi.org/10.1016/S0034-4257(96)00067-3.
Gawuc, L., Jefimow, M., Szymankiewicz, K., Kuchcik, M., Sattari, A., Struzewska, J., 2020. Statistical modeling of Urban Heat Island intensity in Warsaw, Poland using simultaneous air and surface temperature observations. IEEE J. Selec. Top. Applied Earth Observ. Remote Sens. 13, 2716–2728. https://doi.org/10.1109/JSTARS.2020.2989071.
Gharagozlou, A., Tayeba, A., Dadashi, M., Abdolahi, H., 2014. Zoning of CO emissions in Tehran in the medium term by using third quartile as the exposure candidate. J. Geogr. Inf. Syst. 06 (05), 526–532. https://doi.org/10.4236/jgis.2014.65043.
Ghasempour, F., Sekertekin, A., Kutoglu, S.H., 2021. Google earth engine based spatio-temporal analysis of air pollutants before and during the first wave COVID-19 outbreak over Turkey via remote sensing. J. Clean. Prod. 319, 128599 https://doi.org/10.1016/j.jclepro.2021.128599.
Google, 2020. Google COVID-19 Community Mobility Reports. https://www.google.com/covid19/mobility/.
Google Earth Engine, 2012. No Title. https://code.earthengine.google.com/.
Hell, B., Jakobsson, M., 2011. Gridding heterogeneous bathymetric data sets with stacked continuous curvature splines in tension. Mar. Geophys. Res. 32 (4), 493–501. https://doi.org/10.1007/s11001-011-9141-1.
Hengl, T., Heuvelink, G.B.M., Perčec Tadić, M., Pebesma, E.J., 2012. Spatio-temporal prediction of daily temperatures using time-series of MODIS LST images. Theor. Appl. Climatol. 107 (1–2), 265–277. https://doi.org/10.1007/s00704-011-0464-2.
Huang, C., Wang, Y., Li, X., Ren, L., Zhao, J., Hu, Y., Zhang, L., Fan, G., Xu, J., Gu, X., Cheng, Z., Yu, T., Xia, J., Wei, Y., Wu, W., Xie, X., Yin, W., Li, H., Liu, M., Cao, B., 2020. Clinical features of patients infected with 2019 novel coronavirus in Wuhan, China. Lancet 395 (10223), 497–506. https://doi.org/10.1016/S0140-6736(20)30183-5.
Huntington, J.L., Hegewisch, K.C., Daudert, B., Morton, C.G., Abatzoglou, J.T., McEvoy, D.J., Erickson, T., 2017. Climate engine: cloud computing and visualization of climate and remote sensing data for advanced natural resource monitoring and process understanding. Bull. Am. Meteorol. Soc. 98 (11), 2397–2409. https://doi.org/10.1175/BAMS-D-15-00324.1.
Jatim, Pemprov, 2020. Gotong Royong Melawan Covid-19 dalam PSBB di Surabaya, Sidoarjo dan Gresik. Divisi Humas Gugus Tugas Percepatan Penanganan COVID-19 Provinsi Jawa Timur.
Kalisa, E., Fadlallah, S., Amani, M., Nahayo, L., Habiyaremye, G., 2018. Temperature and air pollution relationship during heatwaves in Birmingham, UK. Sustain. Cities Soc. 43, 111–120. https://doi.org/10.1016/j.scs.2018.08.033.
Kanniah, K.D., Kamarul Zaman, N.A.F., Kaskaoutis, D.G., Latif, M.T., 2020. COVID-19's impact on the atmospheric environment in the Southeast Asia region. Sci. Total Environ. 736, 139658 https://doi.org/10.1016/j.scitotenv.2020.139658.
Kim, J.J., Smorodinsky, S., Lipsett, M., Singer, B.C., Hodgson, A.T., Ostro, B., 2004. Traffic-related air pollution near busy roads. Am. J. Respir. Crit. Care Med. 170 (5), 520–526. https://doi.org/10.1164/rccm.200403-281OC.
Kumar, A., Dhakhwa, S., Dikshit, A.K., 2022. Comparative evaluation of fitness of interpolation techniques of ArcGIS using leave-one-out scheme for air quality mapping. J. Geovisual. Spat. Anal. 6 (1), 9. https://doi.org/10.1007/s41651-022-00102-4.
Li, M., Im, J., Beier, C., 2013. Machine learning approaches for forest classification and change analysis using multi-temporal Landsat TM images over Huntington wildlife Forest. GISci. Remote Sens. 50 (4), 361–384. https://doi.org/10.1080/15481603.2013.819161.
Li, P., Feng, Z., Xiao, C., 2018. Acquisition probability differences in cloud coverage of the available Landsat observations over mainland Southeast Asia from 1986 to 2015. Intern. J. Digital Earth 11 (5), 437–450. https://doi.org/10.1080/17538947.2017.1327619.
Li, Q., Guan, X., Wu, P., Wang, X., Zhou, L., Tong, Y., Ren, R., Leung, K.S.M., Lau, E.H.Y., Wong, J.Y., Xing, X., Xiang, N., Wu, Y., Li, C., Chen, Q., Li, D., Liu, T., Zhao, J., Liu, M., Feng, Z., 2020. Early transmission dynamics in Wuhan, China, of novel coronavirus-infected pneumonia. N. Engl. J. Med. 382 (13), 1199–1207. https://doi.org/10.1056/NEJMoa2001316.
Li, W., Ni, L., Li, Z.-L., Duan, S.-B., Wu, H., 2019. Evaluation of machine learning algorithms in spatial downscaling of MODIS land surface temperature. IEEE J. Selec. Top. Appl. Earth Observ. Remote Sens. 12 (7), 2299–2307. https://doi.org/10.1109/JSTARS.2019.2896923.
Lillesand, T.M., Kiefer, R.W., 2000. Remote Sensing and Image Interpretation, 4th ed. John Wiley & Sons.
Londoño-Ciro, L.A., Cañón-Barriga, J.E., 2015. Imputation of spatial air quality data using gis-spline and the index of agreement in sparse urban monitoring networks. Rev. Facul. Ingen. Univer. Antioq. 76 https://doi.org/10.17533/udea.redin.n76a09.
Mandal, I., Pal, S., 2020. COVID-19 pandemic persuaded lockdown effects on environment over stone quarrying and crushing areas. Sci. Total Environ. 732, 139281 https://doi.org/10.1016/j.scitotenv.2020.139281.
Mao, K., Qin, Z., Shi, J., Gong, P., 2005. A practical split-window algorithm for retrieving land-surface temperature from MODIS data. Int. J. Remote Sens. 26 (15), 3181–3204. https://doi.org/10.1080/01431160500044713.
Martinuzzi, S., Gould, W.A., Ramos Gonzalez, O.M., 2007. Creating Cloud-Free Landsat ETM+ Data Sets in Tropical Landscapes: Cloud and Cloud-Shadow Removal. https://doi.org/10.2737/IITF-GTR-32.
Metya, A., Dagupta, P., Halder, S., Chakraborty, S., Tiwari, Y.K., 2020. COVID-19 lockdowns improve air quality in the south-east Asian regions, as seen by the remote sensing satellites. Aerosol Air Qual. Res. 20 (8), 1772–1782. https://doi.org/10.4209/aaqr.2020.05.0240.
Mirsanjari, M.M., Zarandian, A., Mohammadyari, F., Visockiene, J.S., 2020. Investigation of the impacts of urban vegetation loss on the ecosystem service of air pollution mitigation in Karaj metropolis, Iran. Environ. Monit. Assess. 192 (8), 501. https://doi.org/10.1007/s10661-020-08399-8.
Nakada, L.Y.K., Urban, R.C., 2020. COVID-19 pandemic: impacts on the air quality during the partial lockdown in São Paulo state, Brazil. Sci. Total Environ. 730, 139087 https://doi.org/10.1016/j.scitotenv.2020.139087.
Nanda, D., Mishra, D.R., Swain, D., 2021. COVID-19 lockdowns induced land surface temperature variability in mega urban agglomerations in India. Environ Sci Process Impacts 23 (1), 144–159. https://doi.org/10.1039/D0EM00358A.
Naqvi, H.R., Datta, M., Mutreja, G., Siddiqui, M.A., Naqvi, D.F., Naqvi, A.R., 2021. Improved air quality and associated mortalities in India under COVID-19 lockdown. Environ. Pollut. 268, 115691 https://doi.org/10.1016/J.ENVPOL.2020.115691.
Nematchoua, M.K., Orosa, J.A., Afaifia, M., 2022. Prediction of daily global solar radiation and air temperature using six machine learning algorithms; a case of 27 European countries. Ecol. Inform. 69, 101643 https://doi.org/10.1016/j.ecoinf.2022.101643.
Ngarambe, J., Joen, S.J., Han, C.-H., Yun, G.Y., 2021. Exploring the relationship between particulate matter, CO, SO2, NO2, O3 and urban heat island in Seoul, Korea. J. Hazard. Mater. 403, 123615 https://doi.org/10.1016/j.jhazmat.2020.123615.
Nichol, J.E., Fung, W.Y., Lam, K., Wong, M.S., 2009. Urban heat island diagnosis using ASTER satellite images and 'in situ' air temperature. Atmos. Res. 94 (2), 276–284. https://doi.org/10.1016/j.atmosres.2009.06.011.
Pei, Z., Han, G., Ma, X., Su, H., Gong, W., 2020. Response of major air pollutants to COVID-19 lockdowns in China. Sci. Total Environ. 743, 140879 https://doi.org/10.1016/J.SCITOTENV.2020.140879.
Peng, Y., Li, W., Luo, X., Li, H., 2019. A geographically and temporally weighted regression model for spatial downscaling of MODIS land surface temperatures over Urban heterogeneous regions. IEEE Trans. Geosci. Remote Sens. 57 (7), 5012–5027. https://doi.org/10.1109/TGRS.2019.2895351.
Probst, P., Wright, M.N., Boulesteix, A., 2019. Hyperparameters and tuning strategies for random forest. Wiley Interdiscipl. Rev.: Data Min. Knowl. Disc. 9 (3) https://doi.org/10.1002/widm.1301.
Purevdorj, T., Tateishi, R., Ishiyama, T., Honda, Y., 1998. Relationships between percent vegetation cover and vegetation indices. Int. J. Remote Sens. 19 (18), 3519–3535. https://doi.org/10.1080/014311698213795.
Qiu, Z., Ali, M.A., Nichol, J.E., Bilal, M., Tiwari, P., Habtemicheal, B.A., Almazroui, M., Mondal, S.K., Mazhar, U., Wang, Y., Sarker, S., Mustafa, F., Rahman, M.A., 2021. Spatiotemporal investigations of multi-sensor air pollution data over Bangladesh during COVID-19 lockdown. Remote Sens. 13 (5), 877. https://doi.org/10.3390/rs13050877.
R Core Team, 2021. R: A Language and Environment for Statistical Computing (4.1.1). R Foundation for Statistical Computing. https://www.r-project.org/.
Roser, M., Ritchie, H., Ortiz-Ospina, E., Hasell, J., 2020. Coronavirus Disease (COVID-19) – Statistics and Research. Our World in Data. https://ourworldindata.org/coronavirus.
Roy, P.S., Sharma, K.P., Jain, A., 1996. Stratification of density in dry deciduous forest using satellite remote sensing digital data—An approach based on spectral indices. J. Biosci. 21 (5), 723–734. https://doi.org/10.1007/BF02703148.
RStudio Team, 2020. RStudio: Integrated Development Environment for R (1.3.1093). RStudio, Inc. https://www.rstudio.com/.
Schwarz, N., Schlink, U., Franck, U., Großmann, K., 2012. Relationship of land surface and air temperatures and its implications for quantifying urban heat island indicators—an application for the city of Leipzig (Germany). Ecol. Indic. 18, 693–704. https://doi.org/10.1016/j.ecolind.2012.01.001.
Shek, K.Y., Zeren, Y., Guo, H., Li, M., Liu, M., Huang, B., Lyu, X., 2022. Insights on in-situ photochemistry associated with ozone reduction in Guangzhou during the COVID-19 lockdown. Atmosphere 13 (2), 212. https://doi.org/10.3390/atmos13020212.
Shi, Y., Xiang, Y., Zhang, Y., 2019. Urban Design factors influencing surface Urban Heat Island in the high-Density City of Guangzhou based on the local climate zone. Sensors 19 (16), 3459. https://doi.org/10.3390/s19163459.
Shikwambana, L., Kganyago, M., Mhangara, P., 2021. Temporal analysis of changes in anthropogenic emissions and Urban Heat Islands during COVID-19 restrictions in Gauteng Province, South Africa. Aerosol Air Qual. Res. 21 (9), 200437 https://doi.org/10.4209/AAQR.200437.
Simpson, G., Wu, Y., 2014. Accuracy and effort of interpolation and sampling: can GIS help lower field costs? ISPRS Int. J. Geoinf. 3 (4), 1317–1333. https://doi.org/10.3390/ijgi3041317.
Singh, R.P., Chauhan, A., 2020a. Impact of lockdown on air quality in India during COVID-19 pandemic. Air Qual. Atmos. Health 13 (8), 921–928. https://doi.org/10.1007/S11869-020-00863-1/FIGURES/5.
Singh, R.P., Chauhan, A., 2020b. Impact of lockdown on air quality in India during COVID-19 pandemic. Air Qual. Atmos. Health 13 (8), 921–928. https://doi.org/10.1007/S11869-020-00863-1/FIGURES/5.
Toharudin, T., Pontoh, R.S., Zahroh, S., Akbar, A., Sunengsih, N., 2020. Impact of large scale social restriction on the COVID-19 cases in East Java. Commun. Math. Biol. Neurosci. 2020, 1–19. https://doi.org/10.28919/cmbn/4837.
Voogt, J., Oke, T., 2003. Thermal remote sensing of urban climates. Remote Sens. Environ. 86 (3), 370–384. https://doi.org/10.1016/S0034-4257(03)00079-8.
Wan, Zhengming, Dozier, J., 1996. A generalized split-window algorithm for retrieving land-surface temperature from space. IEEE Trans. Geosci. Remote Sens. 34 (4), 892–905. https://doi.org/10.1109/36.508406.

Wang, R., Gao, W., Peng, W., 2020a. Downscale MODIS land surface temperature based on three different models to analyze surface Urban Heat Island: a case study of Hangzhou. Remote Sens. 12 (13), 2134. https://doi.org/10.3390/rs12132134.

Wang, S., Luo, X., Peng, Y., 2020b. Spatial downscaling of MODIS land surface temperature based on geographically weighted autoregressive model. IEEE J. Selec. Top. Appl. Earth Observ. Remote Sens. 13, 2532–2546. https://doi.org/10.1109/JSTARS.2020.2968809.

Wang, Y., Li, Y., Di Sabatino, S., Martilli, A., Chan, P.W., 2018. Effects of anthropogenic heat due to air-conditioning systems on an extreme high temperature event in Hong Kong. Environ. Res. Lett. 13 (3), 034015 https://doi.org/10.1088/1748-9326/aaa848.

WHO. (2020a). Overview of public health and social measures in the context of COVID-19. In Interim Guidance WHO (Issue May). https://www.who.int/publications/i/item/overview-of-public-health-and-social-measures-in-the-context-of-covid-19.

WHO, 2020b. WHO Director-General's Opening Remarks at the Media Briefing on COVID-19 - 11 March 2020. https://www.who.int/dg/speeches/detail/who-director-general-s-opening-remarks-at-the-media-briefing-on-covid-19—11-march-2020.

Wu, H., Li, W., 2019. Downscaling land surface temperatures using a random Forest regression model with multitype predictor variables. IEEE Access 7, 21904–21916. https://doi.org/10.1109/ACCESS.2019.2896241.

Yang, C., Zhan, Q., Lv, Y., Liu, H., 2019. Downscaling land surface temperature using multiscale geographically weighted regression over heterogeneous landscapes in Wuhan, China. IEEE J. Selec. Top. Appl. Earth Observ. Remote Sens. 12 (12), 5213–5222. https://doi.org/10.1109/JSTARS.2019.2955551.

Zha, Y., Gao, J., Ni, S., 2003. Use of normalized difference built-up index in automatically mapping urban areas from TM imagery. Int. J. Remote Sens. 24 (3), 583–594. https://doi.org/10.1080/01431160304987.

Zhao, Y., Nielsen, C.P., McElroy, M.B., Zhang, L., Zhang, J., 2012. CO emissions in China: uncertainties and implications of improved energy efficiency and emission control. Atmos. Environ. 49, 103–113. https://doi.org/10.1016/j.atmosenv.2011.12.015.

Zhao, Z.-Q., He, B.-J., Li, L.-G., Wang, H.-B., Darko, A., 2017. Profile and concentric zonal analysis of relationships between land use/land cover and land surface temperature: case study of Shenyang, China. Energy Build. 155, 282–295. https://doi.org/10.1016/j.enbuild.2017.09.046.